A tonically active master neuron continuously modulates mutually exclusive motor states at two-time scales

Jun Meng[1.2], Tosif Ahamed[2]*, Bin Yu[3], Wesley Hung[2], Sonia El Mouridi[4.5], Zezhen Wang[6], Yongning Zhang[3], Quan Wen[6], Thomas Boulin[4], Shangbang Gao[3]*, Mei Zhen[1.2]*

1. Department of Physiology, University of Toronto, Toronto, ON, Canada
2. Lunenfeld-Tanenbaum Research Institute, Mount Sinai Hospital, Toronto, ON, Canada
3. Huazhong University of Science and Technology, Wuhan, China
4. Univ Lyon, Université Claude Bernard Lyon 1, MeLiS, CNRS UMR 5284, INSERM U1314, Institut NeuroMyoGène, Lyon 69008, France
5. Current address: King Abdullah University of Science and Technology (KAUST), Biological and Environmental Science and Engineering Division (BESE), KAUST Environmental Epigenetics Program (KEEP), Thuwal, 23955-6900, Saudi Arabia
6. Division of Life Sciences and Medicine, University of Science and Technology of China, Hefei, Anhui, China

 * Correspondence

Highlights

- Two mutually exclusive, forward and backward motor states, are inherently asymmetric
- The forward and backward motor states are not separately controlled
- A master neuron underlies continuous modulation and transitions of two motor states
- A tonically active premotor interneuron of the reversal circuit is the master neuron

Abstract

Behaviors consist of distinct states and state transitions. How a neural system continuously modulates each state, which underlies smooth state transitions, is not well understood. *C. elegans* spontaneously switches between two mutually exclusive motor states, forward and backward movements, a behavior long thought to reflect the reciprocal antagonism between interneurons that separately gate the forward and backward motor circuits. We report here that during spontaneous locomotion, the two motor states are not separately controlled, and these interneurons are neither functionally equivalent nor strictly reciprocally inhibitory. AVA, the premotor interneuron previously thought to exclusively gate the backward motor circuit, regulates both motor states with opposite polarities at two-time scales. AVA's transient, fast activation inhibits the forward circuit while initiating the backward movement; in parallel, AVA maintains a slow, but constitutive excitation of the forward circuit to transit from reversals into maintained forward movement. This excitation results from AVA's sustained depolarized membrane potential, which makes its chemical synapse tonically active. A tonically active master neuron breaks the symmetry between the forward and backward motor circuits. It offers an elegant circuit solution for smooth transitions when animals switch between two mutually exclusive motor states.

Introduction

Behaviors are often considered as sequences of discrete motor states. Some states, such as the forward and backward movements, are mutually exclusive[1–11]. Circuit structures such as the winner-take-all and reciprocal inhibition represent a few general solutions that select and promote distinct states[12–16].

However, at shorter timescales, behaviors are less discrete and are more accurately represented as continuously modulated variables, such as the velocity for locomotion[3,17–20]. This is particularly evident when animals switch between mutually exclusive motor states. Indeed, growing experimental evidence shows that the neural network's activity is continuously modulated in behaving animals[21]. Circuit solutions for continuous modulation that underlies smooth transitions between mutually exclusive states are not well understood.

We address this question using the *C. elegans* model system. *C. elegans* exhibits two mutually exclusive motor states: forward movement and backward movement, propelled by the posteriorly and anteriorly propagating undulatory bending waves, respectively. In the absence of explicit sensory stimuli, animals spontaneously switch between the two states[22].

The transition between forward and backward movements has been described by a reciprocally inhibitory neural model: two modules, one for forward movement and one for backward movement[23,24], function separately[25–29]; synaptic connectivity regulates the transition rate and dwell time in each module[6]. This model treats the forward and backward states as mirrored modules; transitions from one to another occur stochastically or through an external input bias.

58   Previous measurements of *C. elegans* locomotion have revealed additional features not

59   captured by this model. Examples include the continuous decay of forward speed prior to the

60   transition into backward movement[6,18,22,30], the period of post-stimulus arousal, during which

61   animals exhibit a higher than pre-stimulus velocity after they exit escape responses[31], and the

62   observation that reducing the activity of premotor interneurons of the backward module

63   decreases not only the backward but also forward speed[32].

64   Here we revisit the relationship between the forward and backward motor circuit during

65   spontaneous locomotion. Anatomically, two groups of non-spiking premotor interneurons, AVB

66   and AVA, make dominant inputs onto two groups of motor neurons that separately execute the

67   forward and backward movements[23,24]. Their functions have been considered to be 'dedicated',

68   with AVB gating the forward motor circuit and AVA gating the backward motor circuit[25–29].

69   However, we found that AVA and AVB are not functionally equivalent and are not strictly

70   reciprocally inhibitory. Instead, AVA, the premotor interneuron that gates the backward motor

71   circuit, has a constitutive and excitatory input on AVB, which activates forward movement. This

72   allows AVA to not only inhibit the forward circuit when it activates the backward movement,

73   but also activate the forward circuit to promote exit from reversals into sustained forward

74   movement. Hence AVA functions as a master neuron to sustain locomotion.

75   These results allude to an inherent asymmetry in a motor circuit that operates with mutually

76   exclusive motor states. We draw this conclusion from evidence revealed by following

77   experimental and modeling studies.

78   First, our whole-cell patch clamp recording revealed that AVA maintains a strongly depolarized

79   membrane potential, whereas AVB does not. A non-spiking neuron's activity is sensitive to

80   changes to its membrane potential. Manipulation of its endogenous K^+ leak leads to controlled

81   perturbation of its activity. When we introduced a further depolarization of AVA by decreasing

82   its K^+ leak, both forward and backward movements are potentiated. With moderate

83   hyperpolarization, both motor states are potently inhibited. These effects are not mirrored by

84   AVB manipulation.

85   These findings prompted us to next evaluate the relationships between AVA and AVB when

86   animals spontaneously locomotion. We found that the calcium and behavior imaging data from

87   wild-type animals fit a simple mathematical model: a fast and inhibitory input and a slow

88   excitatory input from AVA to AVB can predict both AVB activity and animal velocity. This model

89   fits the calcium and behavioral imaging data when AVA becomes further depolarized, but fails

90   when AVA is moderately hyperpolarized. These results postulate that AVA might inhibit or

91   potentiate AVB at different phases of locomotion, an effect that requires AVA to maintain a

92   depolarized membrane potential.

93   These results are consistent with the previous observation that chemogenetic inactivation of

94   AVA reduces overall velocity[32], but not consistent with the previous observation that

95   optogenetic activation of AVA locks the animal in the backward motor state[33–36]. With an

96 optogenetic stimulation protocol that mimics constitutive depolarization, we confirmed that
97 increased AVA activity potentiates overall velocity. With the behavioral effect of titrated
98 chemogenetic inhibition that mimics a sequential hyperpolarization of AVA, we obtained
99 further support on AVA's opposing effect on the forward motor circuit: while AVA's transient
100 depolarization, which initiates backward movements, inhibits forward movement, in parallel,
101 AVA maintains a positive input on the forward circuit to promote forward movement.

102 Finally, through cell and synapse ablation, we showed that AVA potentiates the forward circuit
103 through constitutive acetylcholine release. Thus, by maintaining depolarized membrane
104 potential, AVA maintains an excitatory input onto the forward circuit while gating the backward
105 motor circuit.

106 These results lead to an alternative model. Instead of operating as two equivalent and opposing
107 modules, a tonically active master neuron breaks the symmetry by regulating both forward and
108 backward motor states. A master neuron provides a circuit solution for continuous modulation
109 of velocity during spontaneous transitions between mutually exclusive states.

110 Intriguingly, this master neuron has long been thought to play a singular role in the backward
111 motor circuit. With an inherently higher activity, the reversal module is more frequently evoked
112 during the escape, a behavior essential for survival. Under ambient laboratory conditions, *C.*
113 *elegans* favors forward over backward movement by actively suppressing the reversal module
114 by gap junction-mediated shunting. It makes economic sense for a neural system to make use
115 of the tonic activity of a neuron, primed to execute escapes, to support forward locomotion.

116 **Results**

117 **AVA maintains a more depolarized membrane potential than AVB**

118 AVA and AVB do not fire all-or-none action potentials. Instead, their membrane potentials
119 fluctuate in an analog fashion[6,37,38]. Instead of choosing the lowest value at an arbitrarily
120 estimated steady state as the 'resting' potential, we represent their membrane potentials by
121 the range, as well as the dynamics. The range is shown by cumulative distribution (Fig. 1S1A),
122 and the dynamics by the joint probability distribution of the membrane voltage and its time
123 derivative (Fig. 1S1B).

124 Quantification of our AVA whole-cell patch clamp recording supports the previous conclusion
125 [39–41] that AVA maintains a depolarized potential at multiple stable states. AVA's potential
126 ranged from approximately -30 mV to -10 mV (median -23 mV) (Fig. 1F; Fig. 1SA). Its fluctuation
127 exhibits two regimes with small time derivatives, one from -30 mV to -20 mV, and the other
128 from -15 mV to -10 mV (Fig. 1S1C).

129 In contrast, our recording of AVB revealed a membrane potential at a more hyperpolarized
130 range, approximately from -75mV to -10mV (median -57mV) (Fig. 1S1A). AVB also exhibited
131 dynamic changes in different stable states, most prominently from -75 mV to -45 mV (Fig.

132   1S1B).

133   AVA's membrane properties are consistent with the notion that AVA could remain active even
134   when it is at baseline. At baseline, AVA's potential is near the opening threshold of UNC-2[42], a
135   synaptic high voltage-gated calcium channel that promotes vesicular release[43–45].

An endogenous K⁺ leak current regulates AVA's membrane potential

136   **An endogenous K$^+$ leak current regulates AVA's membrane potential**

137   To understand why AVA is tonically depolarized, we examined the consequence of changing its
138   membrane potential.

139   A neuron's membrane potential can be manipulated by changing its inward and outward leak
140   currents (Fig. 1A). We identified TWK-40, a two-pore domain potassium (K2P) channel, for
141   potential conductance of K$^+$ leak in AVA (Methods; Fig. 1B). Endogenously tagged (Fig. 2S1A)
142   and fully functional (Fig. 2S1B) TWK-40::TagRFP was more abundantly expressed in three
143   neuron classes, AVA, AVB, and DVA, with AVA expression level higher than others (Fig. 1C).
144   TWK-40::TagRFP is present at the plasma membrane of the soma and enriched along the
145   neurite (Fig. 1C).

146   TWK-40 forms a functional K$^+$ leak channel (Fig. 1D). Heterologous expression of TWK-40 in the
147   HEK293T cells led to a small increase of their outward leak current (Fig. 1D), similar to a few
148   mammalian K2P channels [46–48]. A gain-of-function (gf) form, which carries a mutation (L181N)
149   that universally increases K2P channel activity [49,50], led to a large increase in the outward leak
150   current that depends on the intracellular K$^+$ (Fig. 1D).

151   We introduced loss-of-function (lf) and gain-of-function (gf) mutations in *C. elegans twk-40*
152   genomic locus (Fig. 1B; Methods). As expected, AVA exhibited a decreased and increased
153   outward leak current in *twk-40(lf)* and *twk-40(gf)* animals, respectively (Fig. 1E). Consistent with
154   the effect of K$^+$ leak, AVA's membrane potential became further depolarized in *twk-40(lf)* (~-
155   25mV to 0mV), and hyperpolarized in *twk-40(gf)* animals (-40mV to -10mV) (Fig. 1F; Fig. 1S1C).
156   AVA-specific restoration of TWK-40 led to increased outward leak current (Fig. 1E) and
157   hyperpolarization (Fig. 1F; Fig. 1S1C).

Genetic manipulation of leak channel activity perturbs AVA's calcium activity

158   **Genetic manipulation of leak channel activity perturbs AVA's calcium activity**

159   Genetic manipulation of the membrane potential allows for controlled activity perturbation of
160   non-spiking neurons. Indeed, in freely-moving *twk-40(lf)* and *twk-40(gf)* mutants, AVA exhibited
161   increased and decreased overall calcium signals, respectively (Fig. 1S2A). Moreover, consistent
162   with the opposing effects of the inward Na$^+$ leak and outward K$^+$ leak currents on membrane
163   potential, genetic mutations that lead to an increased Na$^+$ leak (*nca-1(gf)*) partially restored the
164   diminished AVA calcium signal in *twk-40(gf)* mutants (Fig. 1S2B).

165   With cell-type specific manipulation of TWK-40 activity, below we investigate the physiological
166   consequence of AVA's depolarized membrane potential, in the context of the intact motor
167   circuit and spontaneous locomotion.

Depolarization of AVA potentiates both backward and forward movements

In the absence of explicit sensory stimuli, wild-type animals spontaneously switch between forward and backward movements (Fig. 2A). *twk-40(lf)* mutants exhibit more frequent transitions into the backward motor state, prolonged reversals, and increased body bending during both reversals and forward movement (Fig. 2B, C). These changes suggest an increase in the animal's overall motor activity.

To assess which neurons contribute to the increased motor activity, we degraded endogenous TWK-40 proteins from sub-groups of TWK-40-expressing neurons using a repurposed ubiquitin-ligase system[51] (Methods; Fig. 2S1A, B). Depleting TWK-40 from AVA alone was sufficient to recapitulate overall increased motor activity (Fig. 2B, C; Fig. 2S1E), while depletion of TWK-40 from AVB, DVA, or additional neurons with minimal expression of TWK-40 (Methods; Fig. 2S1D) had no effect (Fig. 2S1E). When we restored TWK-40 specifically to AVA in *twk-40(lf)* animals, body bending during both forward and backward movements was restored to wild-type levels (Fig.2S1C). Consistently, AVA exhibited increased calcium activity with AVA-specific depletion of TWK-40 (AVA-TWK-40*(*lf*)*), as in *twk-40(lf)* mutants (Fig. 2S2C).

These results were unexpected. Considered as 'dedicated' to the backward motor circuit, AVA should either explicitly regulate the backward circuit, or exert opposite effects on the backward and forward circuits. To further evaluate its role in forward movement, we abolished the animal's ability to reverse by ablating the motor neurons that execute reversals, the A-MNs (Methods). Forward movement was not significantly changed in these animals[25]. However, further ablation of AVA led to significant attenuation of forward movement (Fig. 2S2A). In *twk-40(lf)* mutants, co-ablation of AVA and A-MNs similarly reduced their forward movement (Fig. 2S2A). Thus, further depolarization of AVA potentiates backward as well as forward motor circuit activity.

Hyperpolarization of AVA decreases both backward and forward movement

Mirroring our observation with the *twk-40(lf)* mutants, the *twk-40(gf)* mutation exerts a similar effect for both forward and backward motor states. *twk-40(gf)* mutants exhibit reduced motor activity, with a slightly stronger effect on reversals: forward movement was drastically reduced, and backward movement was abolished (Fig. 2B, C). Furthermore, with AVA-specific TWK-40(gf) expression, AVA's calcium activity was drastically reduced (Fig. 2S2C), and overall motor activity was reduced, with a slightly stronger effect during backward movement (Fig. 2B, C).

These defects could not be explained by a potential developmental effect of hyperpolarization. Indeed, applying an acute, optogenetic silencing of AVA with GtACR2 (Methods), we also observed similarly silenced forward and backward movement (Fig. 2S2B).

Together, AVA's depolarized membrane potential sustains the animal's motility, not only during backward but also forward movements.

AVA's potentiation of forward movement requires AVB

To investigate the circuit mechanism that underlies AVA's potentiation of forward movement, we examined the effect of ablating neurons that have been implicated in either potentiating forward locomotion[27,52] (AVB, PVC) or partitioning the forward and backward motor states[53–58] (RIM) (Fig. 3S1A).

Consistent with previous reports[27,36,59], ablation of AVB significantly reduced forward movement (Fig. 3A). More importantly, ablating AVB in AVA-specific TWK-40(lf) mutants significantly reduced forward movement (Fig. 3B). AVB ablation did not further attenuate the forward movement in AVA-specific TWK-40(gf) mutants, or upon optogenetic hyperpolarization of AVA (Fig. 3S1B, C).

Ablation of other neurons - PVC and RIM - did not attenuate the forward movement of either wild-type animals (Movie S1) or *twk-40(lf)* mutants during spontaneous locomotion (Fig. 3S1A; Movie S2).

AVA positively regulates AVB's activity

To examine how AVA regulates AVB's activity, we directly assessed the amplitude of dynamic change of AVB's membrane potential upon perturbation of AVA (Fig. 3C; Fig. 3S2A).

In wild-type animals, AVB's membrane potential fluctuates between -75mV and -10mV (median -55mV) (Fig. 3S2B, wild-type). When AVA was further depolarized, AVB exhibited a significant increase in the amplitude of potential changes (Fig. 3C; Fig. 3S2A, AVA-TWK-40(lf)), which might correlate with a more depolarized membrane potential range (~-50mV to -10mV, median -32mV) (Fig. 3S2B, AVA-TWK-40(lf)). Conversely, when AVA was hyperpolarized, the dynamic range of AVB's membrane potential changes was drastically reduced (Fig. 3C; Fig. 3S2A, AVA-specific TWK-40(gf)), and AVB exhibited a slight hyperpolarization in the membrane potential range (~-75mV to -30mV, median -58mV) (Fig. 3S2B, AVA-specific TWK-40(gf)).

Consistently, in freely moving animals, AVB's mean calcium activity showed a corresponding increase and decrease when AVA was further depolarized (Fig. 3D, AVA-specific TWK-40(lf)) and hyperpolarized (Fig. 3D, AVA-specific TWK-40(gf)), respectively.

Together, AVA's depolarized membrane potential positively regulates AVB, the premotor interneuron that potentiates forward movement.

Communication from AVA has a more dominant effect on AVB

These results revealed an unexpected, non-antagonizing input from AVA to AVB. We asked whether this effect was reciprocal, specifically, whether AVB might also potentiate AVA.

We examined the effect of AVB inhibition on the backward motor circuit. As expected, optogenetic silencing of AVB reduced the forward movement in moving animals (Fig. 4A; Fig. 4SA) and decreased AVB's calcium activity in immobilized animals (Fig. 4SC). In these animals,

239 the backward movement was unchanged (Fig. 4A; Fig. 4SA), and AVA's activity pattern was
240 similar with or without AVB silencing (Fig. 4C).

241 The lack of an effect of AVB silencing on AVA contrasted with the effect of AVA silencing on
242 AVB. Consistent with the notion that AVA positively regulates AVB's membrane potential and
243 calcium activity, optogenetic inhibition of AVA led to attenuated forward movement in moving
244 animals (Fig. 2S2B; Fig. 4B), and reduced calcium activity in both AVA and AVB (Fig. 4D; Fig.
245 4S1D).

246 These results reveal a more complex relationship between AVA and AVB. Instead of a strict
247 reciprocal inhibition, these experimental findings implicate an asymmetry between the forward
248 and backward motor circuits. During spontaneous locomotion, communication is
249 predominantly from AVA to AVB.

250 **A two-timescale model predicts AVA's regulation of AVB activity**

251 These results raised the need to directly examine the relationship between AVA and AVB
252 neuronal activity, which had not been simultaneously analyzed in freely moving animals[6,26,60].
253 We performed simultaneous calcium imaging of AVA and AVB during spontaneous locomotion
254 and examined their relationship (Methods).

255 For both neurons, the largest activity transients occurred during motor state transitions. As
256 reported[26,27,60–65], each epoch of AVA transients aligned with a transition event. Specifically, the
257 initiation of a reversal coincided with the onset of AVA's calcium rise, whereas the exit from a
258 reversal coincided with the onset of AVA's calcium decay (Fig. 5SA). During this period, AVB's
259 calcium change was anti-correlated with that of AVA (Fig. 5B; Fig. 5SB).

260 This relationship changed after animals began an exit from the reversal. While AVA's activity
261 rapidly decayed to a steady baseline, AVB showed a continued rise as the animal exited the
262 reversal, followed by a slow decay after the animal entered forward movement (Fig. 5B; Fig.
263 5SA). AVA maintained its baseline calcium signals during subsequent forward movement (Fig.
264 5B; Fig. 5SA).

265 We sought the simplest mathematical model that describes this dynamical relationship.
266 Because the functional communication between the two neurons was largely unidirectional
267 (Fig. 4), we considered an input/output model where AVA is treated as the input to AVB. The
268 calcium imaging data suggested a model with two timescales: a fast input during reversals, and
269 a slower one during post-reversals, to account for two phases of AVB activity dynamics. This led
270 to a simple linear dynamical system model (Fig. 5A, upper panel).

$$x_{AVB} = a \cdot x_{AVA} + b \cdot y \qquad (1)$$

$$\frac{dy}{dt} = -\frac{1}{\tau} \cdot y + x_{AVA} \qquad (2)$$

273 where x_{AVB} and x_{AVA} represent the activity of AVB and AVA, respectively; y represents the slow
274 input from AVA (1), given by the leaky-integrator in (2). The model has three free parameters:

7

275 the strength of the fast input, a, the strength of the slow input, b, and the timescale for the
276 slow input, τ.

277 We used the framework of linear systems identification to fit parameters to our calcium
278 imaging data (Fig. 5B; Methods). The best-fit parameters set the strength of fast input a to a
279 negative value and the slow input b to a positive value (Fig. 5D).

280 Biologically, this could be interpreted as the forward circuit receiving input from AVA at two
281 timescales with opposite polarities: a fast inhibitory input and a slow excitatory input. In other
282 words, AVA maintains a constitutive and excitatory input on AVB, in addition to a strong
283 activation-mediated inhibitory input to AVB during transitions. Without the slow excitatory
284 input, the gradual decay of AVB activity after a reversal cannot be predicted by the one
285 timescale model (Fig. 5B, C).

286 With different parameter values, this two-timescale model could also predict the animal's
287 spontaneous velocity from AVA's activity (Fig. 5E), thus capturing the continuous modulation of
288 behavior during state transitions.

289 Together, these results suggest a new model where AVA functions as a master regulator of
290 spontaneous locomotion by bi-directional regulation of AVB at different timescales. A transient
291 but strong depolarization of AVA leads to phasic inhibition during reversals, while a persistent
292 but weak depolarization of AVA provides tonic excitation to AVB that promotes forward
293 movement between reversals (Fig. 5A, lower panel).

294 **Depolarized membrane potential is necessary for AVA's master regulator role**

295 We asked if AVA's master regulator role requires AVA to maintain its membrane potential. We
296 co-imaged AVA and AVB in freely behaving AVA-specific TWK-40(lf) and AVA-specific TWK-
297 40(gf) mutants, and examined their relationships.

298 When we further depolarized AVA (AVA-TWK-40(lf)), the time-dependent relationships with
299 AVB and velocity are maintained (Fig. 5SB; 5SD). The two-timescale model predicted AVB's
300 activity (Fig. 5B-D) and velocity (Fig. 5Gii) from AVA's calcium signals. Parameters for both
301 inputs showed a trend of further increase, but with a slightly higher value for the fast input a
302 (Fig. 5D). Biologically, this suggests that with further depolarization, AVA maintains and
303 strengthens both fast-inhibitory and slow-excitatory inputs (Fig. 5D; Fig. 5SD).

304 In AVA-TWK-40(gf) mutants, the relationship between AVA and AVB activity changed
305 completely such that the model was no longer applicable. Both neurons exhibited drastically
306 reduced calcium signals with little dynamical changes (Fig. 2B, C; Fig. 5SA). In rare cases where
307 AVA exhibited detectable calcium transients, AVB tracked these changes (Fig. 5F), but these
308 transients were not correlated with specific motor states (Fig. 5SC).

309   These results suggest that the two-time scale model for AVA's master regulator role is
310   contingent on its depolarized membrane potential.

311   **A constitutive, minimal optogenetic depolarization of AVA potentiates the forward circuit**

312   Our results reveal AVA's dual modulation – transient inhibition and constitutive excitation – of
313   the forward circuit. Previous optogenetic depolarization of AVA resulted in instantaneous
314   initiation and sustenance of reversals[35,36]. We reasoned that current stimulation protocols only
315   reflect AVA's inhibitory effect on the forward circuit upon strong depolarization (Fig. 6A).

316   To mimic constitutive, weak excitation, we applied a new stimulation protocol to a strain that
317   expresses Chrimson specifically in AVA (Fig. 6B; Methods). Specifically, we pre-conditioned the
318   AVA neuron through a period of activation before we subjected animals to constitutive and
319   minimal light stimulation. These animals recapitulated the motor pattern of AVA-TWK-40(lf)
320   mutants – more frequent transitions and potentiation of both forward and backward
321   movements (Fig. 6B, '+ Con, +ATR'). Without pre-conditioning (Fig. 6B, '- Con, +ATR'), this
322   stimulation increased reversal frequency without potentiating forward movement. Without the
323   co-factor that activates Chrimson (Fig. 6B, '+ Con, -ATR'), light alone did not potentiate either
324   motor state. Consistent with the requirement of AVB for the behavioral effect of AVA's
325   stimulation, in the absence of AVB, this stimulation protocol no longer potentiated the forward
326   movement (Fig. 6S, '-AVB').

327   This result corroborates our conclusion that AVA maintains a weak, but constitutive excitatory
328   input onto the forward motor circuit.

329   **Titrated chemogenetic hyperpolarization isolates AVA's potentiation of the forward circuit**

330   A constitutive input from AVA may reflect a tonic activation of its synaptic activity. We
331   examined this possibility through dosage-dependent chemogenetic hyperpolarization by a
332   histamine-gated chloride channel (HisCl)[31].

333   Exposing animals that ectopically express HisCl in AVA led to a histamine-dependent reduction
334   of reversals, as well as spontaneous forward speed[31]. We further noted that the backward
335   motor circuit exhibited higher sensitivity to histamine (Fig. 6C, D). At 2mM, histamine nearly
336   fully blocked reversals (Fig. 6C) but only modestly reduced forward movement (Fig. 6D). With
337   increased histamine, forward movement progressively declined (Fig. 6D).

338   An implication of this result is that with sequential membrane hyperpolarization, AVA rapidly
339   loses its ability of transient activation that underlies inhibitory input onto the forward circuit,
340   but gradually loses its constitutive activation that underlies excitatory input on the forward
341   circuit.

342   To directly visualize the effect of HisCl on AVA's synaptic activity, we examined the intensity of
343   synaptobrevin/SNB-1::pHluorin, a marker of synaptic vesicle exocytosis[63] along the AVA axon
344   (Fig. 6F; Methods). As expected from increased and decreased vesicular release, *twk-40(lf)* and

345   *twk-40(gf)* mutants exhibited an increased and decreased steady-state fluorescent intensity,

346   respectively (Fig. 6F). In wild-type animals, histamine-induced AVA hyperpolarization led to a

347   dosage-dependent progressive decrease of SNB-1::pHluorin signals (Fig. 6E). These results are

348   consistent with a gradual attenuation of synaptic vesicle release as AVA becomes increasingly

349   hyperpolarized. Importantly, at lower histamine concentrations, which blocked reversals with

350   modest effects on forward movement, SNB-1::pHluorin signals were reduced but remained.

351   Together, our genetic, optogenetic, and chemogenetic perturbation of AVA's membrane

352   potential consistently demonstrates AVA's dual modulation of the forward motor circuit: in

353   parallel to a transient inhibition during reversals, AVA maintains constitutive excitation likely

354   through constitutive synaptic activity.

355   **Tetanus toxin selectively blocks AVA's chemical synaptic transmission**

356   We asked whether AVA's transient and constitutive inputs are mediated through different

357   forms of synaptic transmission. AVA forms both chemical and electrical synapses with other

358   neurons[23,26,66,67]. For chemical synaptic transmission, AVA functions primarily as a cholinergic

359   neuron but also synthesizes multiple neuropeptides[68–70].

360   Tetanus toxin (TeTx) cleaves synaptobrevin/SNB-1 and is commonly used to block chemical

361   synaptic transmission[71,72]. Prior to applying TeTx to block AVA's chemical synaptic transmission,

362   we first asked whether TeTx impairs exocytosis of both synaptic and dense core vesicles, which

363   underlie classic neurotransmitter release and neuromodulator secretion, respectively.

364   We addressed this question by comparing TeTx's effect on a synaptic vesicle marker (SNB-

365   1::GFP) (Fig. 7A) and two neuropeptide markers[73], INS-22::pHluorin (Fig. 7B) and INS-22::GFP

366   (Fig. 7C, D), all expressed in AVA. TeTx, specifically expressed by AVA, diminished the SNB-

367   1::GFP signals at AVA's presynaptic termini (Fig. 7A). In contrast, TeTx did not change the

368   steady-state signals of INS-22::pHluorin, a proxy for dense-core vesicle exocytosis (Fig. 7B). INS-

369   22::GFP signals were increased along AVA's axon (Fig. 7C), but were similarly accumulated in

370   the scavenger cell for secreted peptides (Fig.7D).

371   These results indicate that at least in the AVA neuron, TeTx potently blocks synaptic vesicle

372   release, but has only a minor effect on neuropeptide secretion. This allowed us to attribute the

373   effects of specific expression of TeTx in AVA (below) to impaired chemical synaptic

374   transmission.

375   **Cholinergic transmission underlies AVA's constitutive excitation of the forward circuit**

376   AVA-specific expression of TeTx (AVA-TeTx) led to significant decreases in forward and

377   backward movements, in both wild-type animals and *twk-40(lf)* mutants (Fig. 8S). Because AVA

378   is a cholinergic neuron, we further compared the effect of reducing vesicle loading of

379   acetylcholine by AVA-specific RNA interference (RNAi)[74] against the acetyltransferase CHA-1

380   (Methods[75]). Similar to AVA-TeTx, AVA-specific *cha-1* RNAi led to a reduction of both forward

381   movement (Fig. 8A) and backward movement (Fig. 8SA). Lastly, TeTx fully blocked AVA-

10

382 mediated potentiation of forward movement upon constitutive and minimal optogenetic
383 stimulation (Fig. 8B). These results demonstrate that AVA's potentiation of the forward motor
384 circuit requires cholinergic synaptic transmission.

385 Consistent with its behavioral effect, TeTx disrupted AVA's dynamic relationships with AVB (Fig.
386 8C). In AVA-TeTx animals, AVA continued to exhibit calcium activity transients; however, AVB's
387 activity transient was drastically reduced (Fig. 8SB), disrupting the correlation between AVA and
388 AVB calcium dynamics (Fig. 8C). Occasionally, AVB exhibited activity transients that did not
389 correlate with AVA. Neither AVA nor the rare AVB calcium dynamics showed correlations with
390 velocity (Fig. 8SC).

391 We conclude that AVA's acetylcholine release contributes to both constitutive activation and
392 transient inhibition of the forward motor circuit (Fig. 8D). Critical for this study is a requirement
393 for AVA's tonic cholinergic transmission to potentiate forward movement. The simplest
394 implication is that AVA's strongly depolarized membrane potential supports the constitutive
395 vesicular release of acetylcholine, providing a slow but continuous positive driving force for the
396 forward motor circuit to ensure smooth motor state transitions.

Discussion

398 Our study investigates how a neural system continuously modulates different behavioral states
399 to aid their transitions. *C. elegans* spontaneously switches between forward and backward
400 movements. Despite being mutually exclusive, the two motor states are not independently
401 controlled. Two groups of premotor interneurons separately gate the motor neurons that
402 execute either forward or backward movements, but these interneurons do not strictly
403 antagonize each other. Instead, AVA, the interneuron that gates motor neurons for reversals,
404 regulates AVB, the interneuron that activates motor neurons for forward movement, at two
405 timescales, and with opposite polarities. When AVA activates the reversal motor neurons, a fast
406 but transient inhibitory input to AVB promotes the backward movement. Simultaneously, AVB
407 receives a slow but tonic excitatory input from AVA, which allows transitions from reversals into
408 sustained forward movement. Mechanistically, AVA's tonic excitatory input results from a
409 depolarized membrane potential, which supports constitutive acetylcholine release. This
410 configuration breaks the structural and functional symmetry between the forward and
411 backward motor circuit, making AVA the master regulator of both states (Fig. 8D). A tonically
412 active master neuron offers an elegant circuit solution for continuous behavioral modulation.

Forward and backward motor states are asymmetric

414 *C. elegans* intrinsically switches between the forward and backward motor states, but these
415 two states are not merely mirrored functional modules.

11

416 During spontaneous locomotion, *C. elegans* preferentially sustains forward movement over
417 backward movement, resulting in a higher propensity of the forward state. But when executed,
418 the shorter backward movement exhibits greater vigor than the forward movement[76].

419 Reversal is more frequently evoked and prolonged when animals encounter repulsive stimuli
420 and attempt to escape[22,76,77]. Importantly, evoked reversals potently modify the forward motor
421 state that follows. A prolonged reversal is more likely followed by a turn, a form of forward
422 movement that steers away from the original trajectory, whereas a shorter reversal is more
423 likely followed by forward movement with a similar trajectory, which resembles most
424 spontaneous reversals [76,78–82]. Evoked reversals further increase the forward speed,
425 potentiating the forward state for up to several minutes[83].

426 Reversal thus represents an intrinsically more robust, but actively suppressed motor state; its
427 activation modifies and potentiates the subsequent forward state. Our studies examine neural
428 mechanisms that underlie this inherent asymmetry.

429 **Forward and backward motor states are not separately controlled**

430 Anatomically, the forward and backward motor circuits consist of distinct sets of motor neurons
431 and premotor interneurons, wired with mixed electrical and chemical synapses. Despite the
432 similarity in their wiring configuration, the two motor circuits are not symmetric modules.

433 Neurons that drive backward movement have higher excitability. The premotor interneuron
434 AVA maintains a depolarized membrane potential at ~ -23mV, contrasting with the significantly
435 hyperpolarized potential of the premotor interneuron of the forward circuit (~-55mV).
436 Excitatory motor neurons that execute reversals have higher spontaneous activity than those
437 controlling forward movement[25,27]. These differences corroborate the intrinsic robustness of
438 reversals.

439 Neurons of the backward motor circuit also play a more dominant role in overall motor control.
440 While the two motor states are separately executed by motor neurons in each circuit[25,29], they
441 are not separately regulated by premotor interneurons. AVB is more dedicated to promoting
442 the forward state. In contrast, AVA promotes both motor states. When depolarized, AVA
443 initiates reversals. When at its 'rest' state, it generates a tonic, positive drive for AVB to
444 promote forward movement.

445 AVA being a master regulator aligns with the modification of the forward motor state after
446 evoked reversals. Reminiscent to the functional requirement of an excitation from AVA to AVB
447 during spontaneous transitions, the 'turn' transition to forward movement requires excitation
448 from the backward to the turning module[82].

449 **AVA underlies continuous modulation of motor activity**

450 A master neuron that bi-directionally regulates two mutually exclusive motor states aids
451 spontaneous transitions.

452   Previously, we and others showed that AVA exerts dual modulation of the backward motor
453   circuit[25,26,57]. At its 'rest' state, AVA reduces spontaneous reversals by gap junction-mediated
454   shunting of the motor neurons that execute reversals. At its activated state, AVA initiates
455   reversals via chemical synapse-mediated potentiation of these motor neurons. Here, we show
456   that AVA's chemical synapses exert dual modulation of the forward circuit. At its 'rest' state,
457   AVA steadily potentiates the forward motor circuit through a tonic release of acetylcholine. At
458   its activated state, AVA transiently inhibits the forward circuit.

459   These are complementary effects for overall motor control. When AVA is at 'rest', the forward
460   motor state is stabilized by simultaneous inhibition of the reversal circuit and activation of the
461   forward circuit. Conversely, when AVA is activated, the backward motor state is promoted by
462   simultaneous activation of the reversal circuit and inhibition of the forward circuit (Fig. 8D).

463   Central to AVA's role is its uniquely depolarized membrane potential (Table 1; this study) with a
464   mixed wiring configuration. Being intrinsically depolarized, its gap junctions actively suppress
465   the backward motor state, while its intrinsic excitability allows for phasic, but robust reversals.
466   Being tonically depolarized, a baseline release from its chemical synapses slowly but tonically
467   potentiates forward movement. With opposing effects on both motor circuits at different
468   timescales, AVA underlies continuous modulation of both motor states.

469   Our model is derived from experimental data from spontaneous locomotion. The proposed
470   configuration, with minimal feedback from AVB, likely represents a minimal functional module.
471   When sensory inputs impose changes to locomotion, reciprocal feedback between AVA and
472   AVB, and with other interneurons in the backward and forward modules, should be recruited to
473   modify the relationship between forward and backward movement. However, the inherent
474   asymmetry between the two motor states should always impose a more dominant effect from
475   the reversal motor circuit.

476   **Premotor interneurons of the reversal circuit regulate overall motor activity**

477   It is intriguing that the premotor interneuron of the backward, but not the forward circuit, plays
478   the dominant role in overall motor control. Reversals are driven by a robust but actively
479   suppressed circuit. The motor system finds an economical solution by using the same tonic
480   drive to shunt backward and potentiate forward locomotion. This solution allows animals to
481   generate robust escape responses. Moreover, AVA's tonic input to AVB, an integrated copy of
482   its activity with slow decay, might serve as a short-term memory of the history of internal states
483   and environment.

484   **Partial convergence between anatomic and functional connectivity**

485   AVA's regulation of the forward circuit cannot be directly deduced from the anatomical wiring.
486   In the wiring diagram, AVA does not make stereotypic direct synaptic inputs to AVB, whereas
487   AVB makes stereotypic synaptic inputs to AVA[23,84,85].

488   There are several potential explanations. The simplest is that AVA's synaptic connections with
489   other interneurons relay its effects on AVB. The wiring diagram offers two candidates, RIM and
490   PVC, that connect the forward and backward motor circuit. Indeed, our ablation of RIM or PVC
491   led to an increased spontaneous reversal, an effect consistent with RIM-specific chemical
492   synapse ablation[52,55,57,78], but these animals maintain coordinated forward-backward transitions
493   and spontaneous velocity. Their ablation did not reduce the overall motor activity in *twk-40(lf)*
494   mutants either. A multi-synapse explanation cannot be excluded but seems unlikely.

495   Instead, we favor a mechanism in which AVA's tonic acetylcholine release facilitates extra-
496   synaptic accumulation and potentiation of the forward motor circuit. Indeed, in the developing
497   larvae, extrasynaptic cholinergic transmission from premotor interneurons provides the tonic
498   potentiation of ventral muscles that functionally substitute for the missing ventral subcircuit[86].

499   Importantly, systematic surveys of functional connectivity upon single neuron optogenetic
500   stimulation revealed extensive discrepancies between the anatomic chemical synaptic wiring
501   and functional connectivity throughout the *C. elegans* nervous system[87,88]. Partial correlations
502   between anatomic wiring and activity patterns were similarly noted in other systems[89–92].

503   Other forms of functional communication - ephaptic coupling, extrasynaptic transmission,
504   modulatory signaling – might compensate for the limited number of anatomic wiring in a small
505   neural system. However, the more interesting intuition is that the form of 'invisible' wiring
506   might be preferentially utilized for spontaneous behavioral states, whereas anatomic wiring,
507   such as AVB to AVA, is built mainly for contextual recruitment for evoked behaviors or decision-
508   making. Essentially, it is another economical form of wiring by a small neural system.

509   **Dynamic regulation of a non-spiking neural network**

510   With a few exceptions[93,94], the *C. elegans* neural system consists primarily of non-spiking
511   neurons[37,40,41,95–99]. This neural network generates behaviors that are stable, flexible, and
512   adaptive, as neural networks that function through regenerative potentials.

513   AVA's functional model suggests that precise and dynamic regulation of the activity of non-
514   spiking neurons and their network can be achieved through the precise modulation of
515   membrane potentials. *C. elegans* exceptional expansion of K^+ channels, in particular, the 47 K^+
516   leak channels[49,100–102] might serve this role. When a neuron functions through graded potential
517   changes, it is particularly suited for a K2P conductance to regulate its activity range and form of
518   responses to stimuli[100,103]. With 47 K2P genes expressed by overlapping subgroups of 300
519   neurons[69], these channels could define the unique computational properties of each neuron.
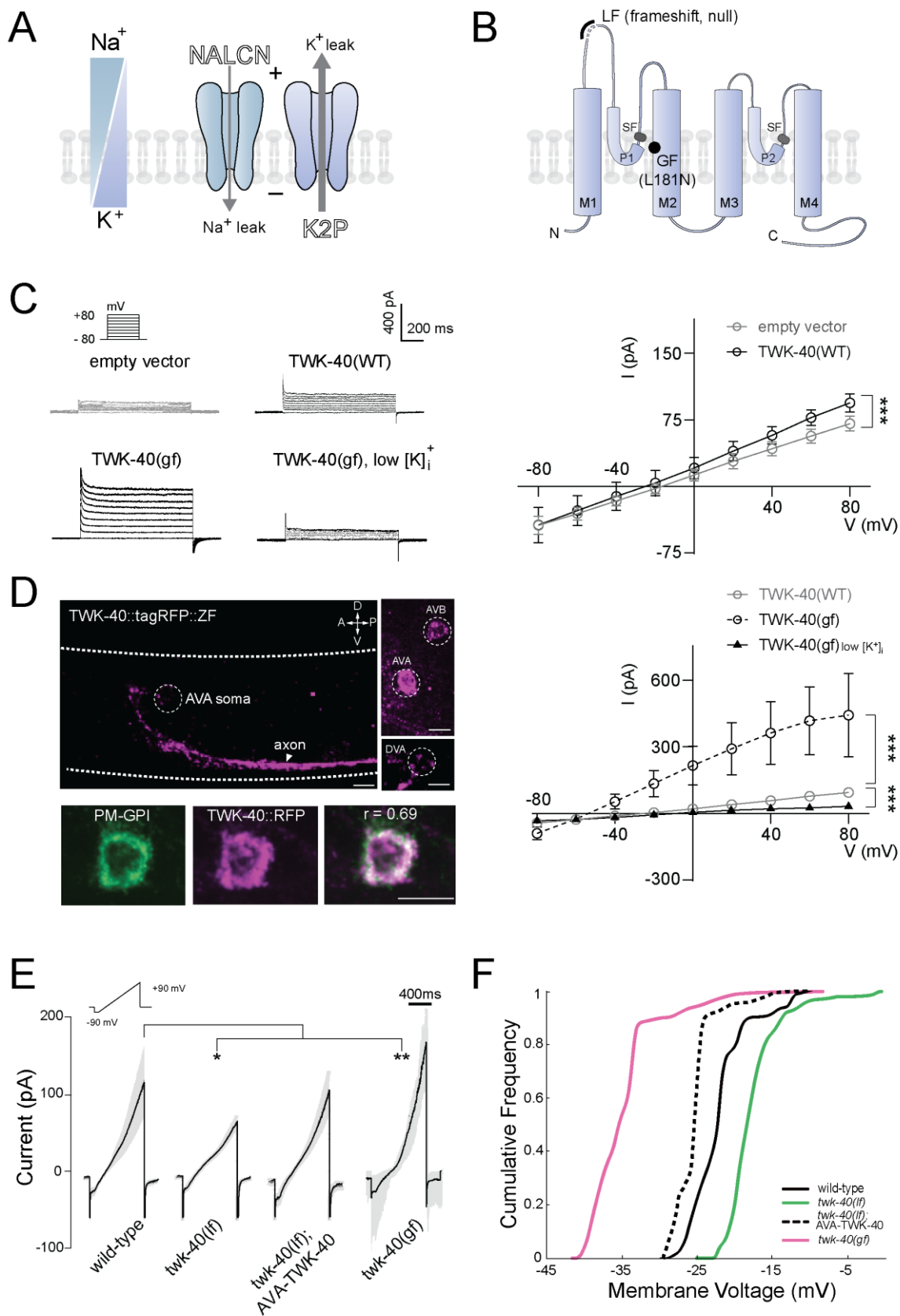
520

521 **Figure 1. The K2P channel TWK-40 regulates AVA's membrane potential.**

522 A. Schematics of the inward sodium and outward potassium leak currents and respective leak
523   channels that contribute to a neuron's negative membrane potential.

524 B. Schematics of the predicted topological structure of TWK-40 (isoform b) with denoted
525   genetic mutations. LF: loss-of-function. A null allele (*hp834*) has a 7bp deletion that leads to
526   truncation after the first transmembrane domain (M1). GF: Gain-of-function. *bln336* (L181N)
527   has an activating mutation that promotes the conductance of all K2P channels.

528 C. (Left) Representative step currents from HEK293 cells carrying different heterologous
529   expression vectors by whole-cell voltage-clamp recording. (Right), I-V curve for respective
530   cells with mean and 95% CI. Quantification showed average currents at +80 mV. Upper
531   panel: Cells expressing wild-type TWK-40 (n=13) showed a small outward current compared
532   to the cell with empty vector (n=12); Lower panel: Cells expressing TWK-40(GF) showed a
533   larger current (n=10), which was diminished by reducing intracellular K^+ concentration from
534   140 mM to 14 mM (n=7). * denotes statistical significance.

535 D. Expression pattern of endogenously tagged TWK-40::tag RFP. (Upper panels), maximum
536   intensity projection of confocal images of TWK-40::tagRFP. Dashed lines outline the animal.
537   Somas are denoted by circles. The arrowhead labels processes along the ventral nerve cord.
538   Scale bar, 2μm. (Lower panel) TWK-40::tagRFP co-localizes with a plasma membrane marker.
539   r: Pearson's correlation.

540 E. AVA's leak current was recorded by whole-cell patching, with a ramping potential from -
541   60mV to +90mV. Black traces and gray areas denote mean and range. Currents at +80mV
542   were compared. N = 5 (wild-type), 8 (*twk-40(lf)*) (n=8)*,* 7 (*twk-40(lf);* AVA-TWK-40) and 7
543   (*twk-40(gf)*). * denotes statistical significance.

544 F. Cumulative fraction of AVA's membrane potential with no current injection in wild-type
545   (n=7), *twk-40(lf)* (n=9), *twk-40(lf);* AVA-TWK-40 (n= 9) and *twk-40(gf)* (n=13) animals.
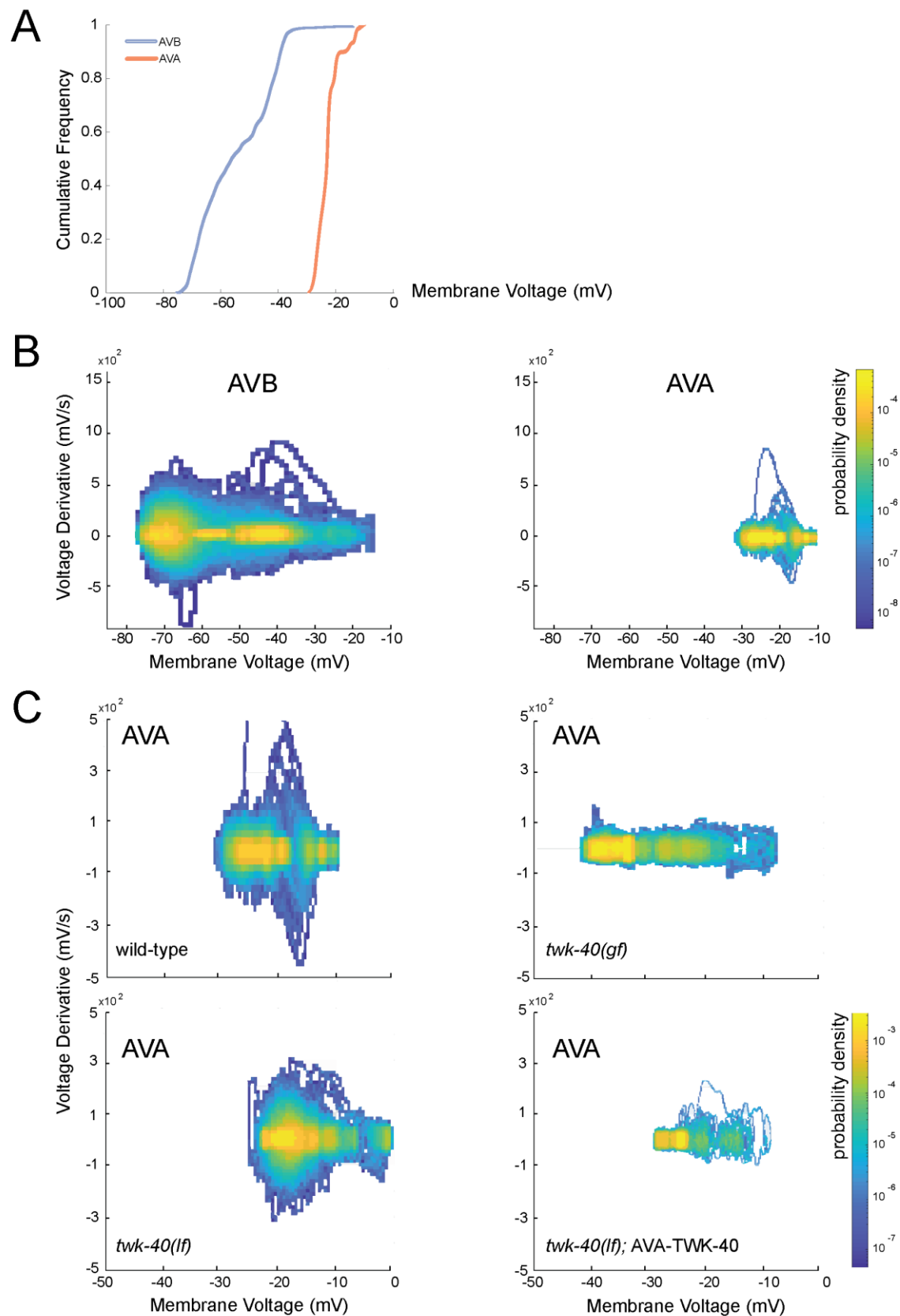546   respectively, compared to wild-type (n=7) animals.

16

547

17

Figure 1S1. TWK-40 regulates AVA's membrane potential.

A. AVA holds a more depolarized membrane potential than AVB. Cumulative frequency of the membrane potential of AVB (n=8) and AVA (n=7), with no current injection.

B. AVA and AVB exhibit relatively steady potentials at different voltages. The dynamic range of potential changes for AVB (n=8) and AVA (n=7), is shown by the distribution of voltage derivatives across their membrane potentials.

C. Changing K^+ leak changes both the range and the dynamic range of AVA's membrane potential. Distribution of voltage derivatives across AVA's membrane potentials shows an increase and decrease of the range and dynamic range in *twk-40(lf)* (n=9) and *twk-40(gf)* (n=13) animals, respectively. AVA-specific restoration of TWK-40 in *twk-40(lf)* mutants (n=8) decreased AVA's membrane potential and reduced the dynamic range, similar to *twk-40(gf)* mutant animals.
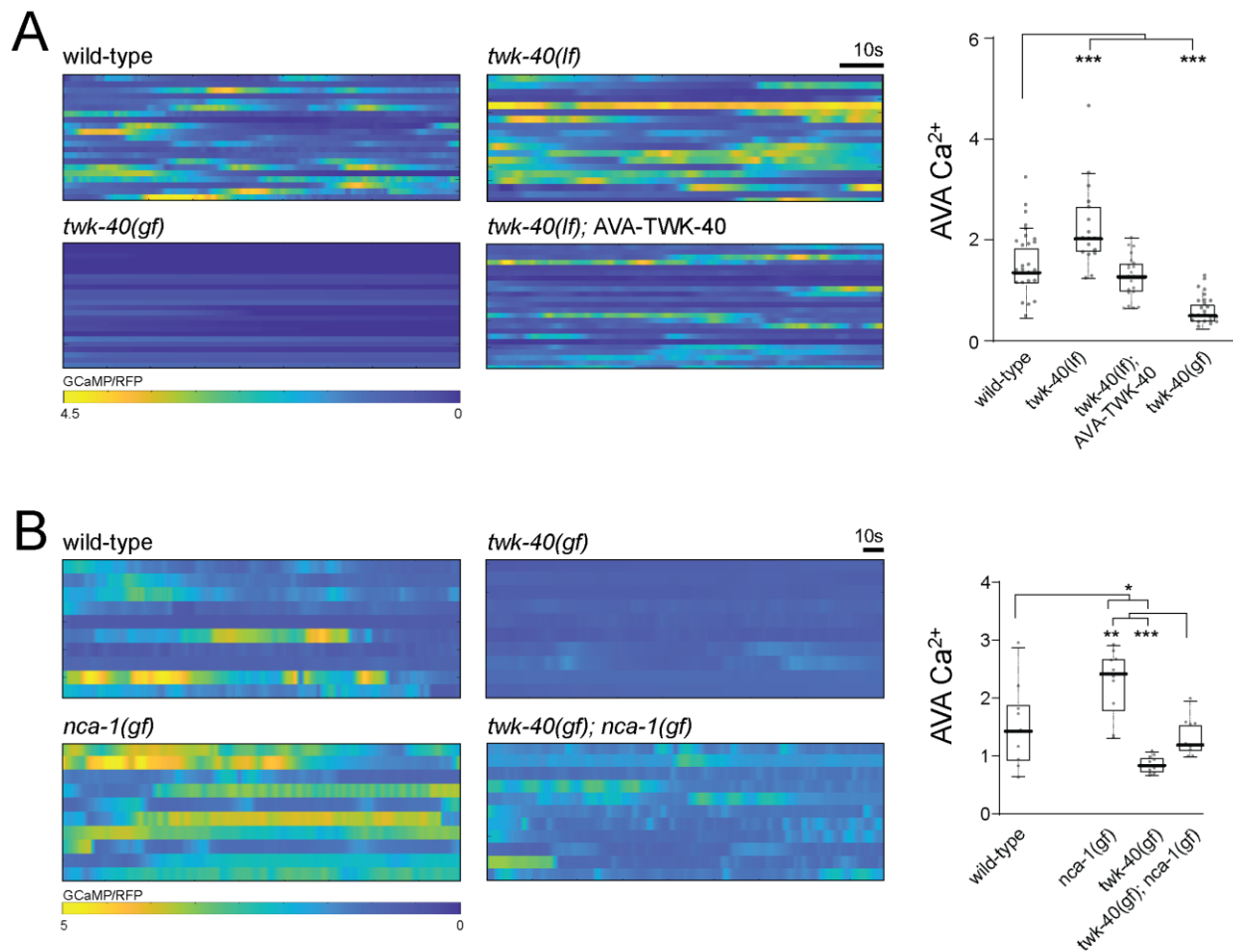
560

Figure 1S2. Genetic interactions between the TWK-40 K$^+$ leak and NCA Na$^+$ leak channel mutants corroborate an antagonizing effect on AVA activity.

A. Raster plots (left panels) and quantification (right panels) of AVA soma calcium activity in freely moving wild-type (n=20), *twk-40(lf)* (n=17), *twk-40(lf);* AVA-specific TWK-40 (n=24) and *twk-40(gf)* (n=24) animals. Each trace in the raster plot represents the recording of one animal over time. GCaMP/RFP ratio denotes calcium activity; * denotes statistical significance.

B. Raster plots (left panels) and quantification (right panel) of AVA soma calcium activity in freely moving animals of denoted genotype. Consistent with their motor phenotypes[104], increasing Na$^+$ leak (*nca-1(gf)*, n=9) correlates with increased AVA calcium activity than wild-type animals (n=10), and partially compensated for AVA's activity dampened by increased K$^+$ leak (*twk-40(gf); nca-1(gf),* n=11). GCaMP/RFP ratio denotes calcium activity; * denotes statistical significance.

575
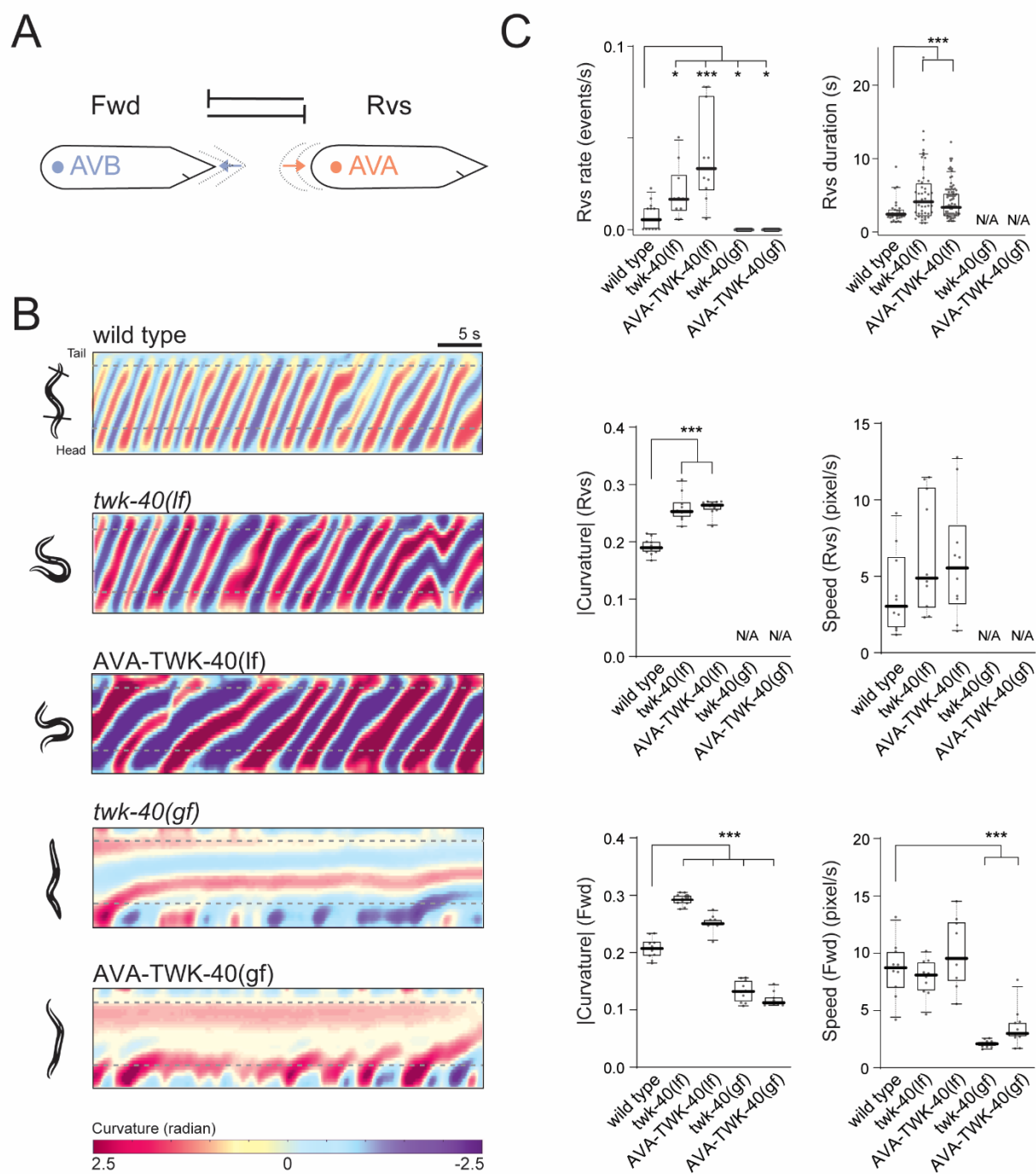
576 **Figure 2. AVA regulates both forward and backward movements.**

577 A. Mutual exclusion between the forward (Fwd) and backward (Rvs) motor states is considered
578   to reflect the reciprocal antagonisms between AVB and AVA, the respective principal
579   premotor interneurons of the forward and backward motor circuit.

580 B. Representative kymograph of bending curvature of a freely moving animal of denoted
581   genotype. Segments between dashed lines denote the body. A bending wave from head to
582   tail over time denotes forward movement, and from tail to head backward movement.
583   Deeper colors denote higher curvatures. *twk-40(lf)* and AVA-specific TWK-40(lf) animals
584   show increased curvature. *twk-40(gf)* and AVA-specific TWK-40(gf) animals exhibit severely
585   diminished body bending.

586 C. Quantification of initiation rate of reversals, centroid velocity, and body curvature. (Top)
587   Averaged reversal rates (Rvs, left) and reversal duration (right) exhibited by animals of
588   denoted genotypes. *twk-40(lf)* (n: 46 events from 11 animals) and AVA-specific TWK-40(lf)
589   (80 events from 11 animals) animals exhibit increased Reversal rates and duration compared
590   to wild-type animals (30 events from 13 animals). (Middle) Mean absolute body curvature
591   and speed during forward movement by animals of denoted genotypes. (Bottom) Mean
592   absolute body curvature and speed during backward movement. n: 11 (wild type), 11 (*twk-*
593   *40(lf)*), 11 (AVA-specific TWK-40(lf)), 11 (*twk-40(gf)*) and 12 (AVA-specific TWK-40(gf))
594   animals. N/A: no events.

595

596

23

Figure 2S1. TWK-40 functions primarily through AVA to regulate body curvature

A. Genomics structures of *twk-40* and predicted three isoforms (a, b, and c). Blue boxes and lines denote exons and introns, respectively. Red and green boxes denote the C-terminal insertion of TagRFP and ZF domains.

B. Mean absolute bending curvature (left panel) and speed (right panel) of wild-type (n=11) and *twk-40::TagRFP::ZF* (n=11) animals. Insertion of TagRFP::ZF does not change locomotion.

C. Mean absolute bending curvature during forward (left) and backward (right) movement in respective genotypes. AVA-specific restoration of TWK-40 expression in *twk-40(lf)* mutants (n=11) decreased *twk-40(lf)* mutant's curvature (n=10) to wild-type level (n=11). "-" denotes the absence of a transgene that drives TWK-40 expression in AVA. "+" denotes the presence of a transgene that drives TWK-40 expression in AVA. * denotes statistical significance.

D. Immuno-staining of a strain carrying an integrated, functional, multi-copy TWK-40::GFP fosmid array against GFP revealed 18 classes of neurons with different levels of expression. Scale bar, 2μm.

E. Mean absolute curvature during forward movement exhibited by animals with cell-specific depletion of TWK-40. "-": in the absence of ZIF-1, a ubiquitin ligase that degrades *twk-40::RFP:ZF*, animals exhibited wild-type-like bending. "all": expressing ZIF-1 in all TWK-40-expressing neurons led to increased bending, similar to *twk-40(lf)* mutants. The mean curvature of animals expressing ZIF-1 in denoted TWK-40-expressing neurons showed that those included AVA led to increased curvature. * denotes statistical significance.

617

25

618 **Figure 2S2. AVA maintains forward movement.**

619 A. Ablation of AVA in the absence of motor neurons of the reversal motor circuit led to
620   reduced bending and speed during forward movement. Representative kymograph of
621   bending curvature (left panels), averaged absolute body curvature (middle panels) and
622   averaged speed (right panels) upon co-ablation in wild-type (control, n=13; ablated, n=11)
623   and *twk-40(lf)* (control, n=11; ablated, n=11) background are shown. * denotes statistical
624   significance.

625 B. Representative kymograph of bending curvature (left), mean absolute curvature, and
626   velocity in non-stimulated (-ATR) (n=28) and stimulated (+ATR) animals that express GtACR2
627   specifically in AVA (n=25). Curvature and forward speed were reduced during stimulation.
628   Lines and shaded bars denote the median and 95% confidence interval, respectively. *
629   denotes statistical significance.

630 C. Raster plots (left) and quantification (right) of an overall AVA calcium activity (GCaMP/RFP
631   ratio) in freely moving animals. Each trace represents one animal. AVA-specific TWK-40(lf)
632   (n=23) and AVA-specific TWK-40(gf) (n=27) animals exhibit increased and decreased mean
633   calcium activity, respectively, compared to wild-type animals (n=23). * denotes statistical
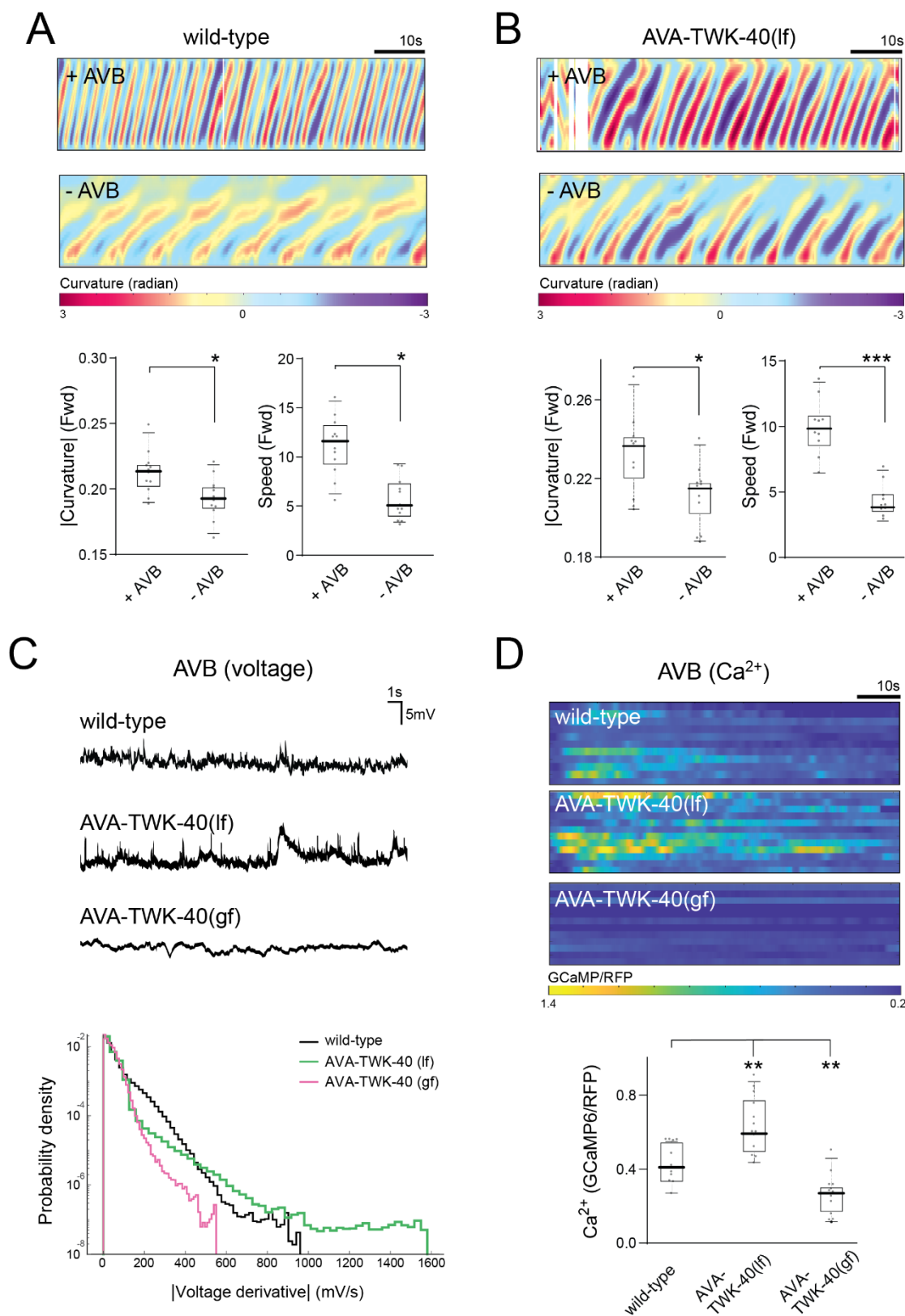634   significance.

635

27

Figure 3. AVA positively regulates AVB's activity

A. Ablation of AVB led to significantly reduced curvature and speed during forward movement of wild-type animals. (Upper panel) Representative kymograph of body curvature of control (+AVB) (n=13) and AVB ablated (-AVB) animals (n=13). (Lower panel) Mean absolute curvature and speed during forward movement by animals of respective genotypes. * denotes statistical significance.

B. Ablation of AVB led to significantly reduced curvature and speed during forward movement of AVA-specific TWK-40(lf) animals. (Upper panel) Representative kymograph of body curvature of control (+AVB) (n=11) and AVB ablated (-AVB) animals (n=11) in AVA-specific TWK-40(lf) mutant animals. (Lower panel) Mean absolute curvature and speed during forward movement by animals of respective genotypes. * denotes statistical significance.

C. (Upper panel) Representative AVB membrane potential recording of respective genotypes in the absence of current injection. (Lower panel) Quantification of AVB membrane potential changes when AVA's membrane potential was changed. AVB exhibited increased and decreased dynamics in AVA-specific TWK-40(lf) (n=7) and AVA-specific TWK-40(lf) (n=8) mutant animals, respectively, compared to wild-type animals (n=8).

D. Raster plot (Upper panel) and quantification (lower panel) of AVB calcium activity during forward movement, in freely moving wild-type (n=12), AVA-specific TWK-40(*lf*) (n=14), and AVA-specific TWK-40(gf) animals (n=13). Each trace represents one animal. AVB exhibited increased and decreased activities in AVA-TWK-40(lf) and AVA-specific TWK-40(gf) animals, respectively, compared to wild-type animals. * denotes statistical significance.

658

29
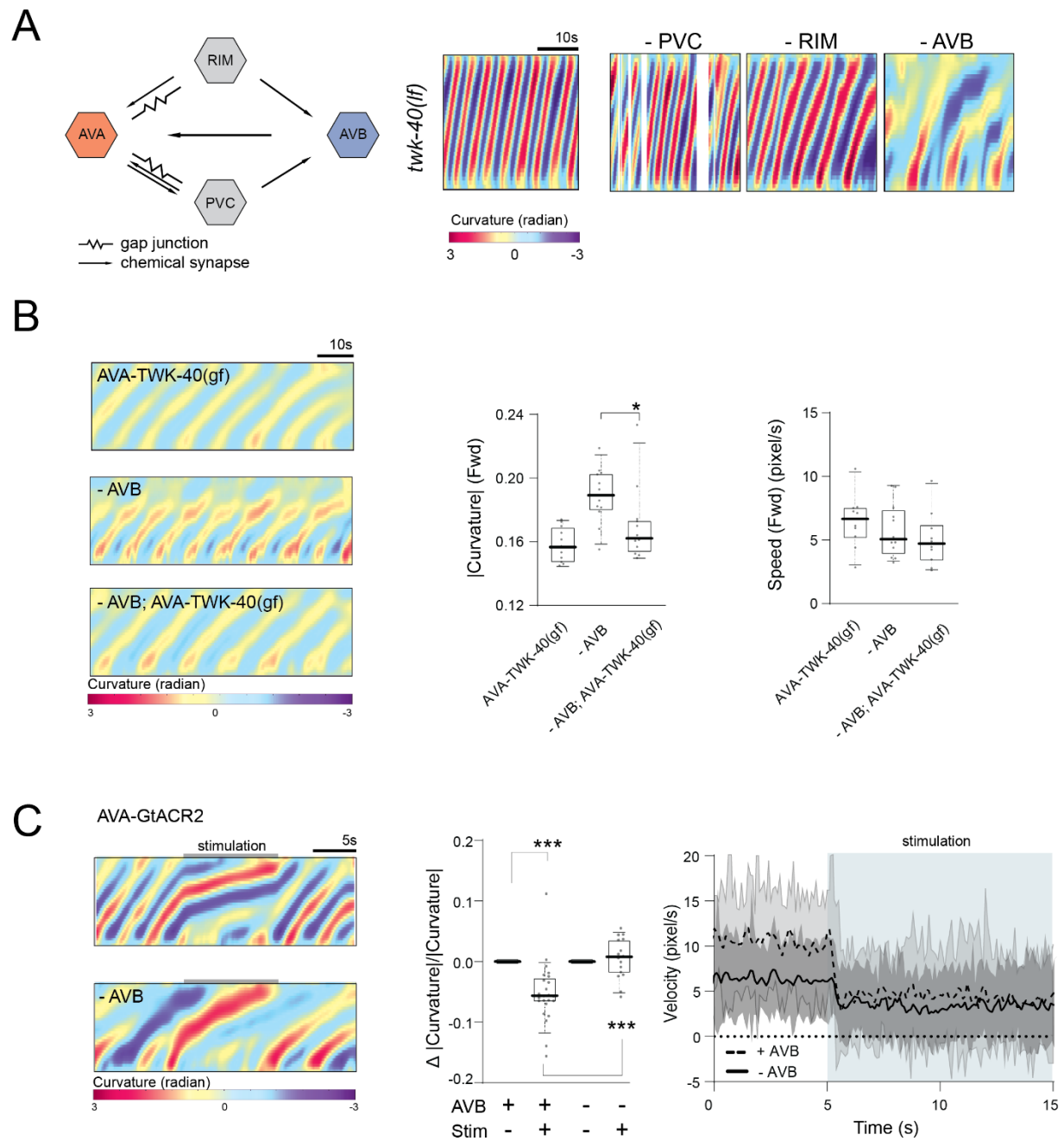
**Figure 3S1. AVA's effect on forward movement requires AVB**

A. (Left) Anatomic connectivity between AVA and AVB. (Right) Representative kymograph of bending curvature of *twk-40(lf)* animals, upon ablation of neurons that make chemical and/or gap junction connections with AVA, -PVC, -RIM, -AVB, in *twk-40(lf)* mutant animals, Only AVB ablation led to decreased bending.

B. (Left) Representative kymograph of bending curvature. (Middle) Mean absolute curvature during forward movement for AVA-specific TWK-40(*gf*) (n=11), AVB ablated (-AVB) wild-type animals (n=13), and AVB ablated AVA-TWK-40(*gf*) animals (n=11). (Right) Averaged forward speed of animals with respective genotypes. Ablating AVB did not cause significant further attenuation of the forward movement of AVA-specific TWK-40(gf) animals. * denotes statistical significance.

C. (Left) representative kymograph of bending curvature of wild-type (+AVB) (n=25) and AVB ablated (-AVB) animals (n=17) upon weak stimulation of GtACR2 expressed specifically in AVA. (Middle and right panel) Mean forward speed and absolute curvature of animals of denoted genotype. Ablation of AVB partially blocked the inhibitory effect of AVA-specific GtACR2 activation on forward movement. Lines and shaded bars denote the median and 95% confidence interval, respectively. * denotes statistical significance.

676
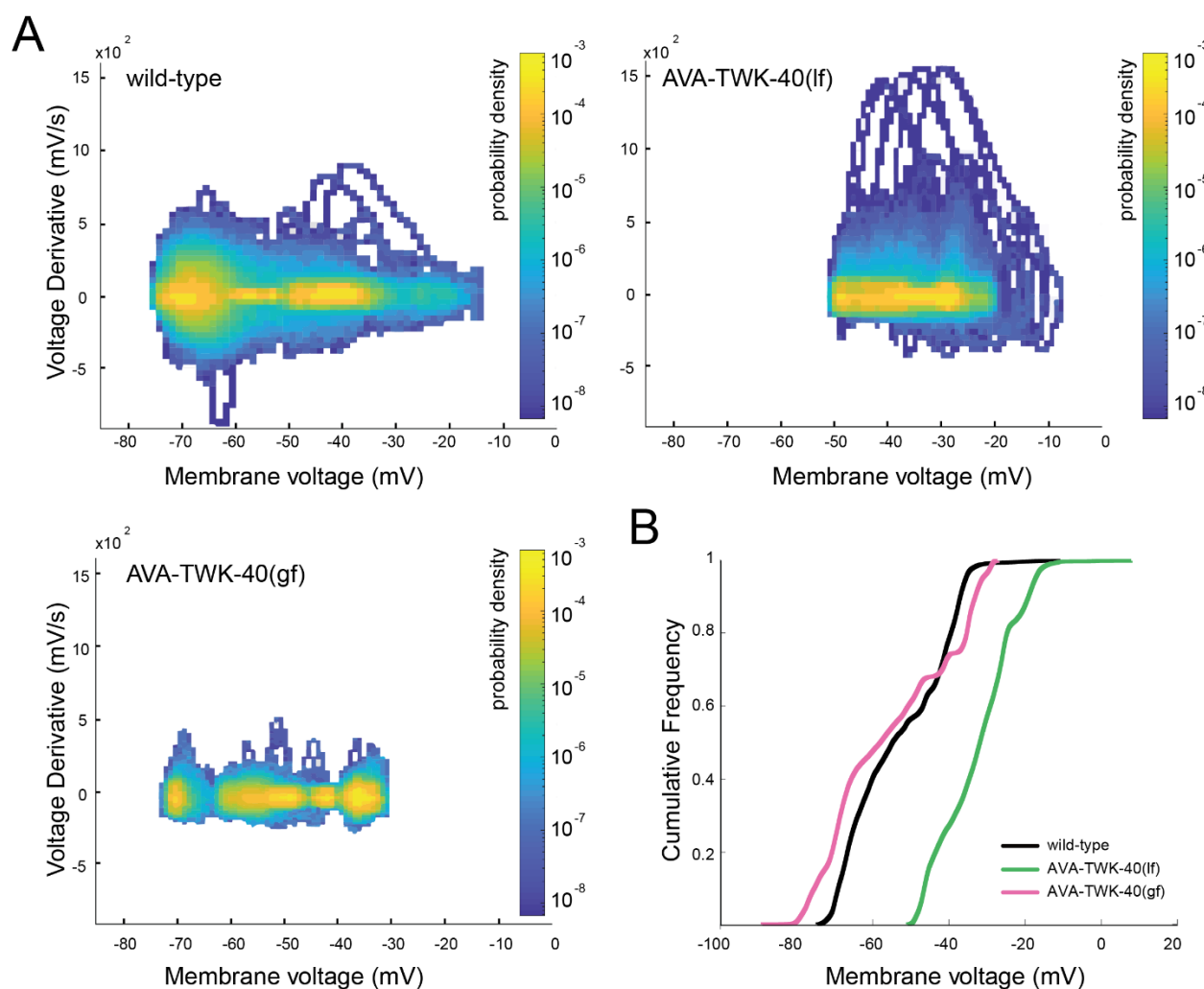
677 **Figure 3S2. AVB's membrane potential and voltage dynamics are positively regulated**
678 **by AVA**

679 A. Distribution of the voltage derivatives across AVB membrane potential in respective
680   genotypes. AVA-specific TWK-40(*lf*) (n=7) and AVA-specific TWK-40(*gf*) (n=7) led to increased
681   and decreased voltage dynamic ranges, respectively, compared to wild-type animals (n=8).

682 B. Cumulative fraction of AVB membrane potential. AVA-specific *twk-40(lf)* (n=7) and AVA-
683   specific *twk-40(gf)* (n=7) led to a more depolarized and hyperpolarized potential range,
684   respectively, compared to wild-type animals (n=7) for AVB.

685
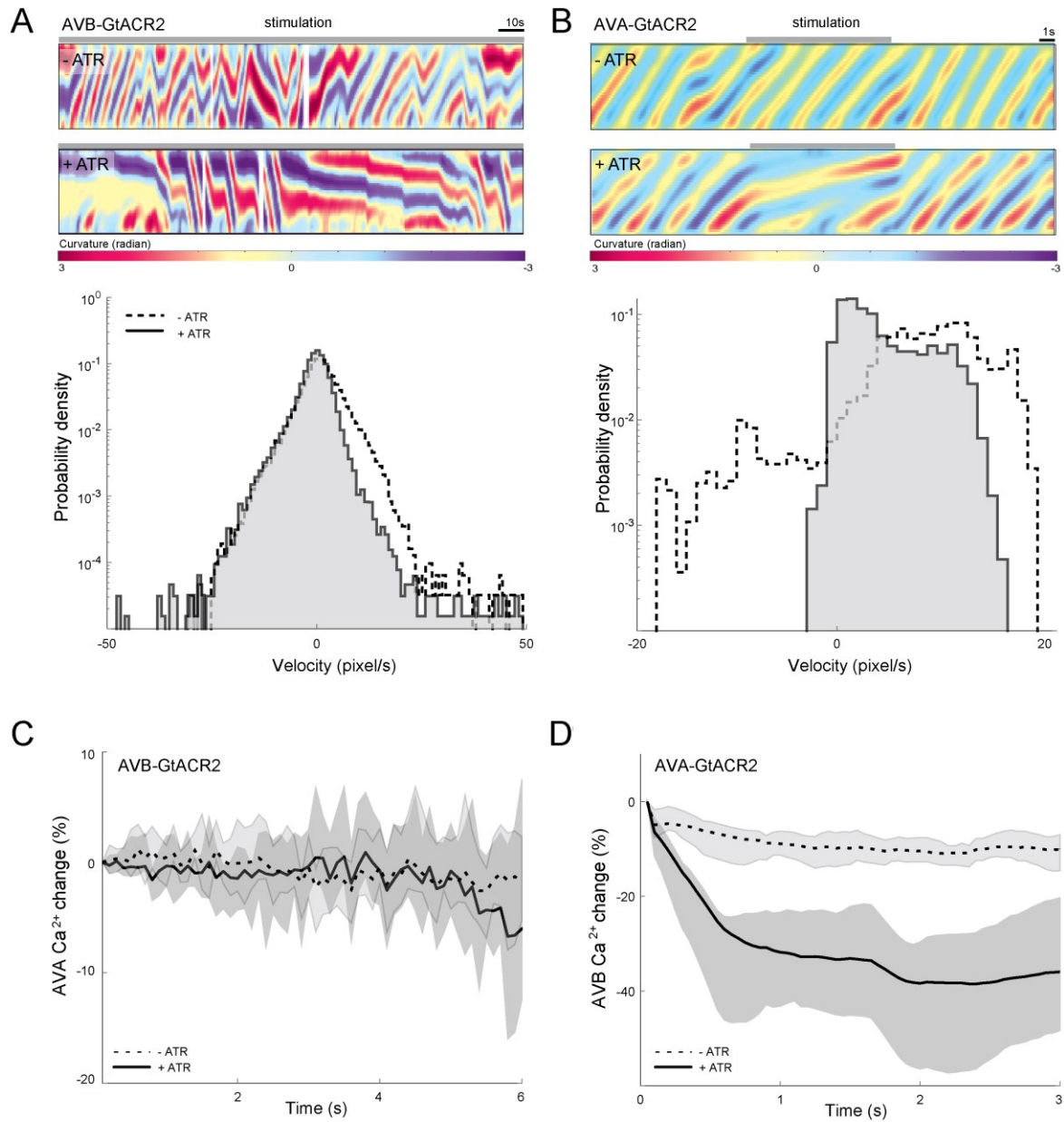
686

Figure 4. Asymmetry in AVA-AVB communication.

A. Representative kymographs (per panel) and normalized probability density (lower panel) of body curvature upon optogenetic silencing by AVB by GtACR2. Silencing AVB (ATR+, n=11) led to decreased forward speed without affecting backward movement compared to non-stimulated animals (-ATR, n=5).

B. Representative kymographs (upper panel) and normalized probability density (lower panel) of bending curvature of animals pre-, during, and post-optogenetic silencing of AVA by GtACR2. Silencing AVA (+ATR, n=28) led to decreased forward speed and diminished backward movement compared to un-stimulated (-ATR, n=25) animals.

C. AVA calcium activity in immobilized animals upon optogenetic silencing of AVB by GtACR2. Inactivation of AVB (+ATR, n=28) did not lead to obvious changes in AVA calcium dynamics compared to un-stimulated animals (-ATR, n=19). Lines and shaded bars denote the median and 95% confidence interval, respectively.

D. AVB calcium activity in immobilized animals upon optogenetic silencing of AVA by GtACR2. Inactivation of AVA (+ATR, n=23) led to reduced AVB calcium dynamics compared to un-stimulated animals (-ATR, n=23). Lines and shaded bars denote the median and 95% confidence interval, respectively.

34

704

35
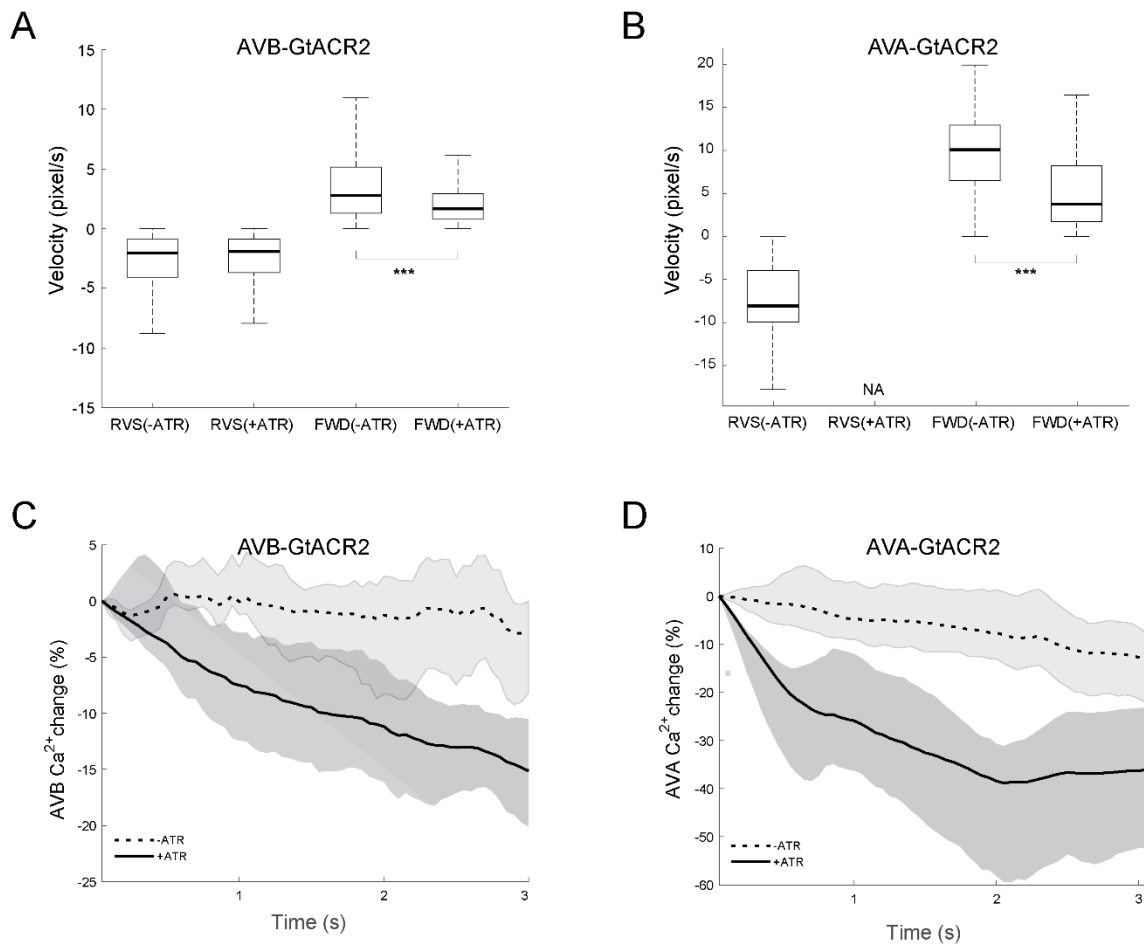
Figure 4S. Asymmetry in AVA-AVB communication.

A. AVB silencing by optogenetic stimulation (+ATR, n=11) led to decreased forward speed (Fwd) without affecting backward speed (Rvs) compared to un-stimulated (-ATR, n=5) animals. * denotes statistical significance.

B. AVA silencing by optogenetic stimulation (+ATR, n=28) led to decreased forward speed (Fwd) and abolished backward movement (Rvs, NA) compared to un-stimulated (-ATR, n=25) animals. * denotes statistical significance.

C. Optogenetic silencing of AVB by GtACR2 in immobilized animals led to reduced AVB calcium activity (+ATR, n=28) compared to un-stimulated (-ATR, n=19) animals. Lines and shaded bars denote the median and 95% confidence interval, respectively.

D. Optogenetic silencing of AVA by GtACR2 in immobilized animals led to reduced AVA calcium activity (+ATR, n=23) compared to unstimulated (-ATR, n=23) animals. Lines and shaded bars denote the median and 95% confidence interval, respectively.

718

37
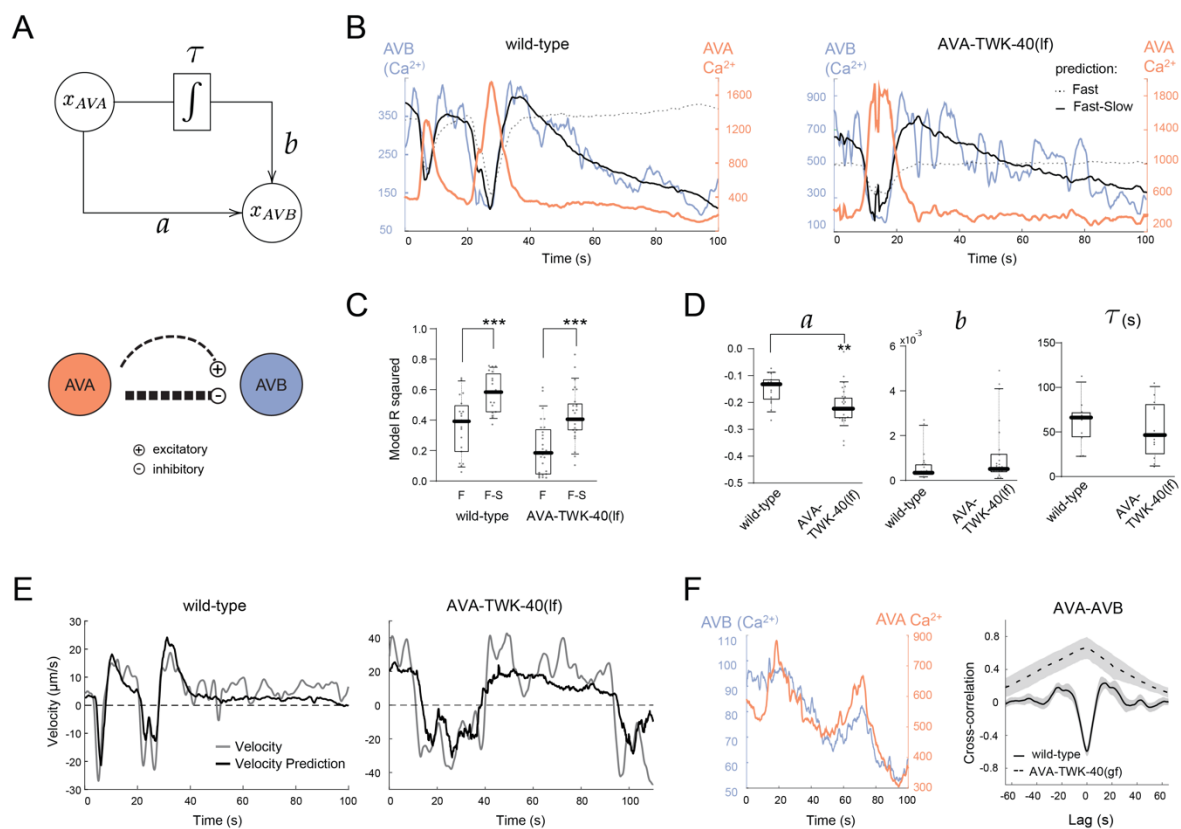
Figure 5. A two-time scale model captures AVA's relationship with AVB and velocity.

A. (Top) AVB activity is modeled as a sum of two terms dependent on AVA's activity. A fast-negative copy with a proportionality constant a and a slow positive copy integrated with a timescale τ and proportionality constant b. (Bottom) Biologically, the two-time scale model suggests a fast inhibition and a slow excitation from AVA to AVB.

B. (Left) Example calcium traces of co-imaged AVA and AVB in freely moving animals show that in the wild-type animal, the fast-slow model is a better fit for AVB's post-reversal activity compared to a model without the slow timescale. (Right) Example calcium traces of AVA and AVB from AVA-specific TWK-40(lf) animals show that the fast-slow model also explains AVB's activity when AVA was further depolarized.

C. Model R-squared values comparing the performance of the fast-slow model with the fast models in wild-type and AVA-specific-40(lf) animals. Removing the slow time scale decreases model performance in both cases. * denotes statistical significance.

D. Comparison of the estimated value for parameters a, b, and the integration timescale for the slow copy τ between wild-type and AVA-specific TWK-40(lf) traces. n= 11 (wild type) and 10 (AVA-specific TWK-40(lf)) reversal events. WT=11 animals, AVA-specific TWK-40(lf)=13 animals. * denotes statistical significance.

E. Sample traces of the model prediction of the velocity of wild-type (Left) and AVA-specific TWK-40(lf) (Right) animals from AVA calcium activity. Wild-type parameters: $a = -0.51, b = 0.02, \tau = 3.5s$; AVA-specific TWK-40(gf) parameters: $a = -0.38, b = 0.004, \tau = 16.6s$.

F. AVA-specific-TWK-40(gf) negatively affects AVA and AVB activity. (Left) Rare calcium traces for AVA and AVB in AVA-specific-TWK-40(gf) mutants showed a strong positive correlation. (Right) Cross-correlation between residual AVA and AVB calcium activities showed a more positive correlation for AVA-specific TWK-40(gf) (n = 13 events, 11 animals) than wild-type (n=29 events, 11 animals).
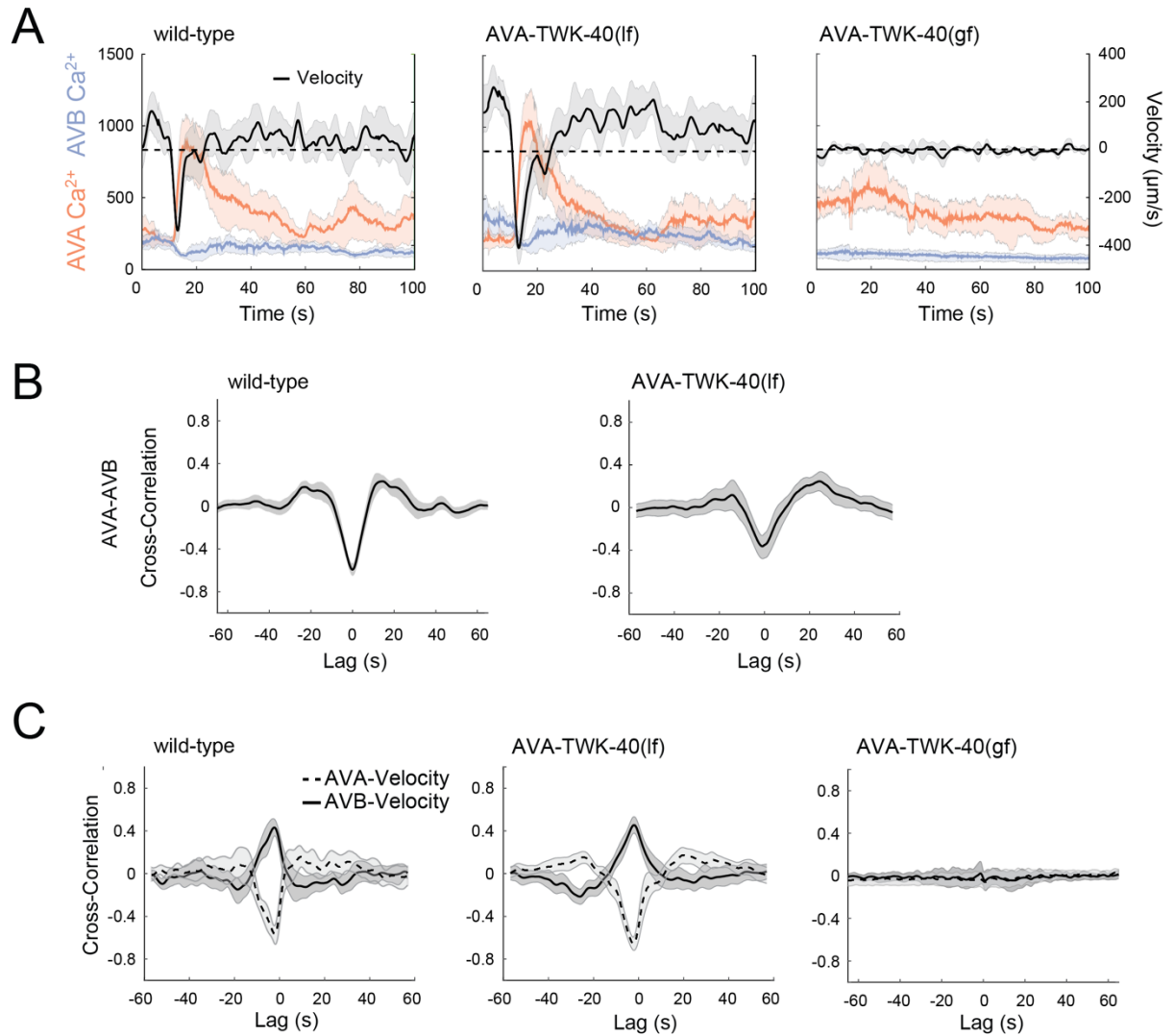
744

**Figure 5S. A two-time scale model captures the AVA-AVB calcium relationship.**

A. Average calcium activity of AVA (orange trace) and AVB (blue trace), aligned to the start of an AVA transient for wild-type, AVA-specific TWK-40(lf), and AVA-specific TWK-40(gf) animals, respectively. Velocity (green trace) is plotted in the right y-axis. . n (events): 19 (wild-type), 27 (AVA-specific TWK-40(lf), 4 (AVA-specific TWK-40(gf)). Lines and shaded bars indicate 95% confidence interval of the mean.

B. Averaged cross-correlations between AVA-AVB calcium activity for wild-type and AVA-specific TWK-40(lf) animals.

C. Averaged cross-correlations between AVA calcium activity and velocity, and AVB calcium activity and velocity, for wild-type, AVA-specific TWK-40(lf), and AVA-specific TWK-40(gf) animals.

756

41
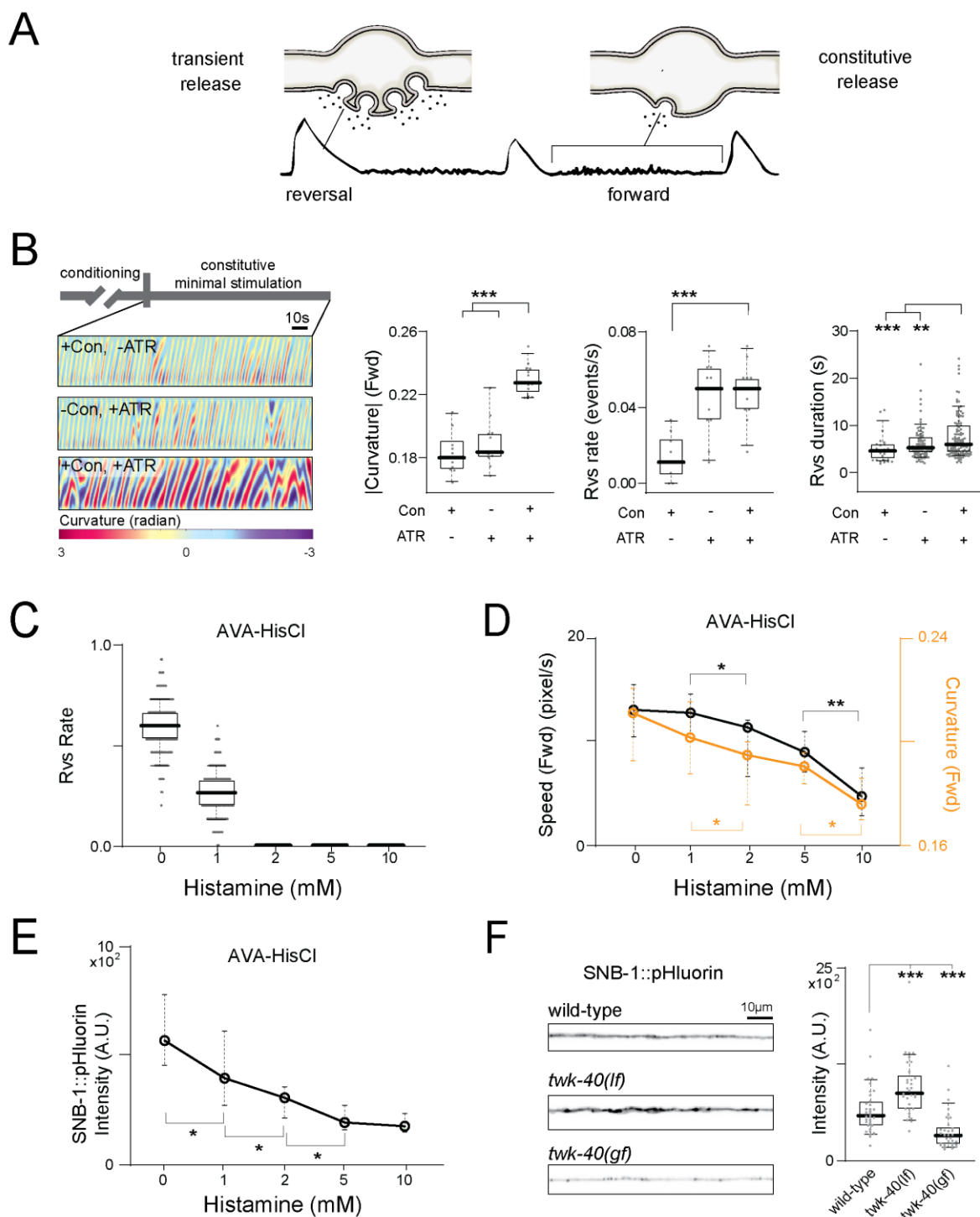
**Figure 6. AVA regulates forward movement through chemical synaptic transmission.**

A. Schematics of the transient versus constitutive neurotransmitter release from AVA.

B. (Left) Representative curvature kymographs of AVA-specific optogenetic activation, with pre-conditioning but no stimulation (+Con, -ATR, n=10), with stimulation without pre-conditioning (-Con, +ATR, n=10), and with stimulation after pre-conditioning (+Con, +ATR, n=14). (Right) Averaged absolute forward curvature, reversal rate, and reversal duration under each condition. Animals with weak stimulation exhibited only an increased reversal rate. Animals with constitutive, minimal stimulation exhibited increased reversal rate and forward curvature. * denotes statistical significance.

C. Exposing AVA-HisCl animals to histamine-impaired spontaneous reversals (Rvs). n=15 animals for each concentration. 2mM histamine diminished spontaneous reversals.

D. Forward speed (left) and absolute curvature (right) at different histamine concentrations showed a gradual reduction with increased histamine (n=15 animals per concentration). * denotes statistical significance.

E. Averaged AVA-SNB-1::pHluorin fluorescent signals at different histamine concentrations showed a gradual increase with increased histamine. n: 30 (0 mM), 29 (1 mM), 30 (2 mM), 31 (5mM), 28 (10 mM). * denotes statistical significance.

F. Schematics, representative image, and quantification of AVA-specific SNB-1::pHluorin signals in wild-type (n=34), *twk-40(lf)* (n=32), and *twk-40(gf)* (n=32) animals. pHluorin signals were significantly increased and decreased in *twk-40(lf)* and *twk-40(gf)*, respectively, compared to wild-type animals. * denotes statistical significance.

778
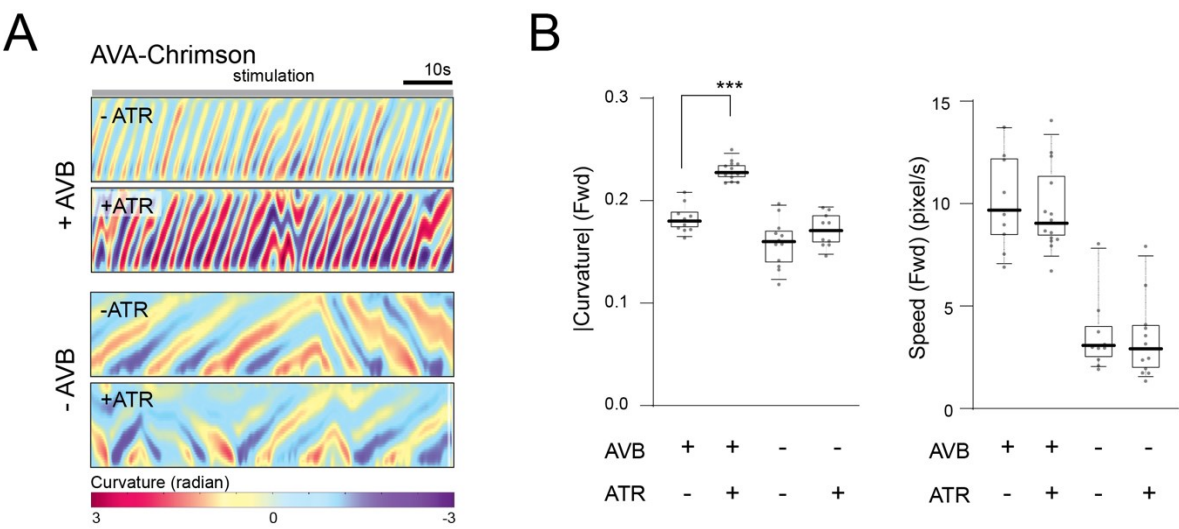
779 **Figure 6S. AVA's constitutive activation of forward movement requires AVB**
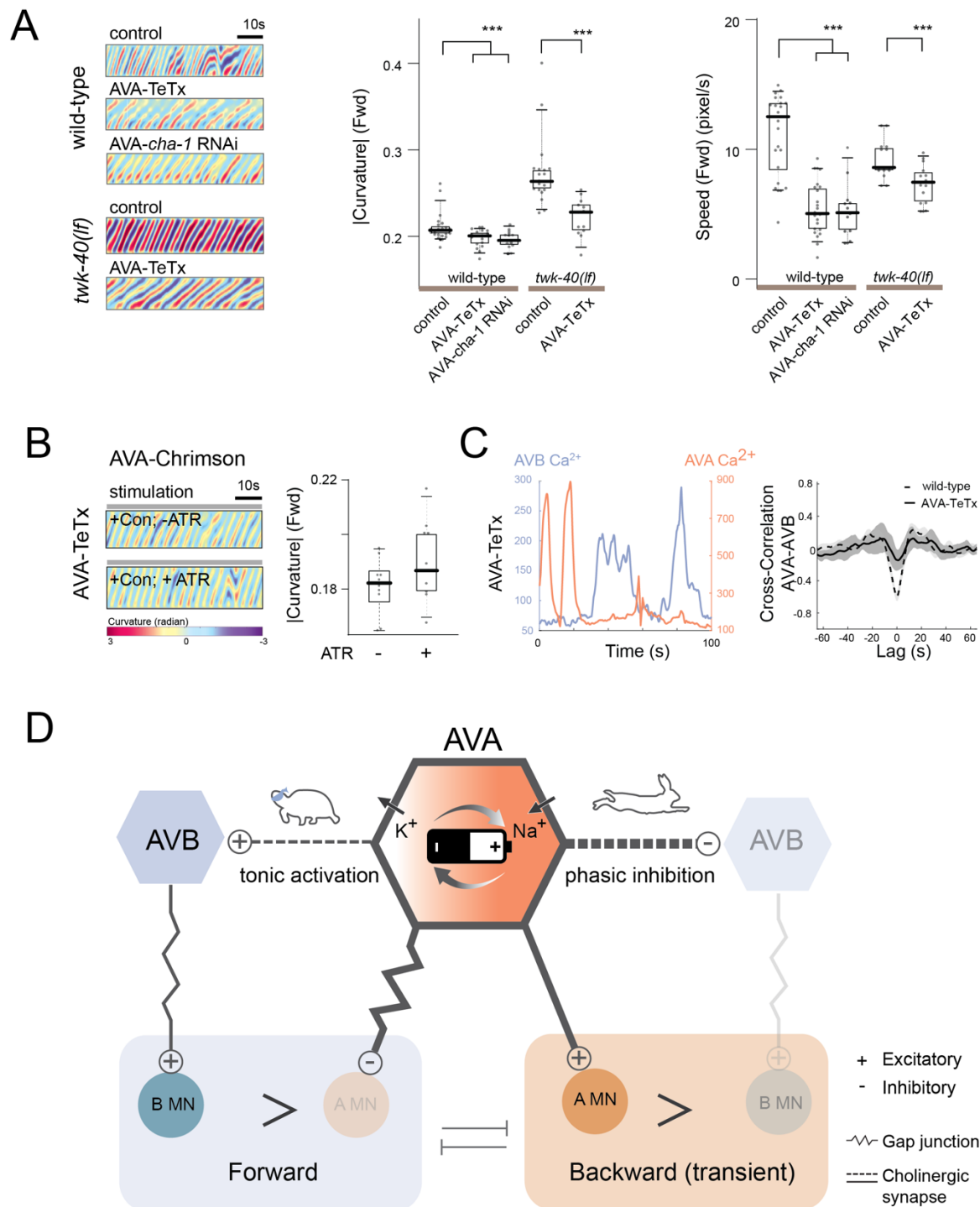
780 A. Representative curvature kymographs of AVA-specific Chrimson animals upon a constitutive
781 and minimal AVA activation (+ATR), with (+) or without (-) the premotor interneuron AVB. -
782 ATR, no stimulation controls.

783 B. Averaged absolute curvature (left) and speed (right) during forward movement upon AVA's
784 constitutive and minimal activation, with (+) or without (-) AVB. Upon AVB Ablation (-AVB),
785 constitutive and minimal activation of AVA no longer induced an increase in the forward
786 movement. n: 10 (+AVB; -ATR, no stimulation), 13 (+AVB; +ATR, with stimulation), 12 (-AVB, -
787 ATR, no stimulation), and 10 (-AVB; +ATR, with stimulation). * denotes statistical
788 significance.
789
790
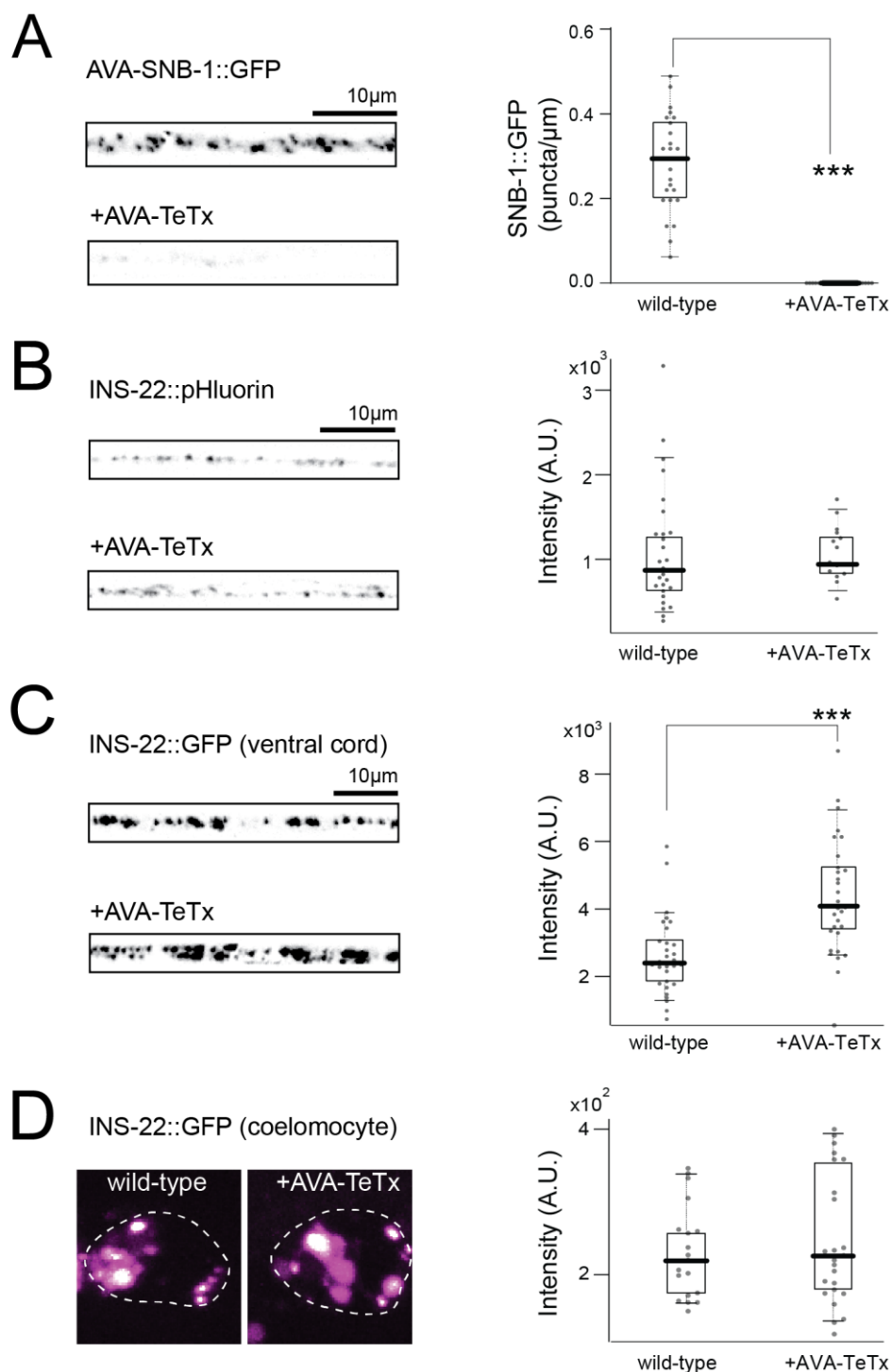
791

Figure 7. TeTx does not significantly impair neuropeptide secretion from AVA

A. Representative images (left) and quantification (right) of SNB-1::GFP signals from AVA in wild-type animals and animals that express AVA-specific TeTx. SNB-1::GFP signals were diminished in the presence of TeTx (n=22) compared to wild-type animals (n=25). * denotes statistical significance.

B. Representative images (left) and quantification (right) of the INS-22::pHluorin signals from AVA showed no significant changes in the presence of AVA-specific TeTx (n=15) compared to wild-type animals (n=27).

C. Representative images (left) and quantification (right) of signals from a neuropeptide marker INS-22::GFP from AVA. Averaged INS-22::GFP intensity of each puncta (right) showed an increase of fluorescent intensity in the presence of AVA-specific TeTx (n=30) compared to wild-type animals (n=30). * denotes statistical significance.

D. Representative images (left) and quantification (right) of INS-22::GFP signals in coelomocytes, which accumulate secreted neuropeptides. Averaged INS-22::GFP intensity showed no difference between wild-type (n=20) and AVA-specific TeTx (n=26) animals.

Figure 8. Cholinergic signaling underlies AVA's regulation of forward movement

A. Representative curvature kymographs (left), averaged absolute curvature (middle), and averaged speed (right), during forward movement by animals with blocked synaptic vesicle fusion (AVA-TeTx), or blocked acetylcholine loading (AVA-cha-1 RNAi) from AVA. Curvature and speed were reduced in AVA-specific TeTx in both wild-type and *twk-40(lf)* animals. AVA-*cha-1* RNAi had a similar effect on forward movement as AVA-TeTx. n: 23 (Control, wild type), 18 (AVA-specific TeTx, wild type), 14 (AVA-*cha-1* RNAi, wild type), 20 (Control, *twk-40(lf)*), 14 (AVA-specific TeTx, *twk-40lf)*). * denotes statistical significance.

B. (Left panels) Representative curvature kymographs upon AVA's constitutive and minimal stimulation (+ATR) in the presence of TeTx. Animals of the same genotype were treated with the same treatment but with opsin-activating factor (-ART) served as controls. (Right panels) Averaged absolute forward curvature. When synaptic vesicle fusion was blocked, stimulation of AVA (+ATR) resulted in no significant changes in forward movement compared to non-stimulated (-ATR) animals. n: 10 (-ATR), 11 (+ATR).

C. (Left) Example calcium traces of co-imaged AVA and AVB in freely moving AVA-specific TeTx animals. (Right) Cross-correlation of co-imaged AVA and AVB showed reduced anti-correlation in AVA-specific TeTx animals (n=10) compared to wild-type animals (n=19).

D. AVA functions as a master regulator to modulate forward and backward movement and coordinate their transitions. (Left side) At a lower activity state, AVA actively shunts reversal motor neuron A by gap junction-coupling [26]. At this state, AVA's tonic acetylcholine transmission potentiates AVB to activate the B motor neurons for sustained forward movement. (Right side) When AVA is at a high activity state, its phasic activation inhibits AVB while potentiating A motor neurons by transient acetylcholine transmission to initiate backward movement. Arrows between the low and high AVA states denote continuous modulations of velocity during transitions between the mutually exclusive motor states. Dashed and straight lines denote extrasynaptic/indirect and synaptic connectivity, respectively. Line thickness denotes synaptic strength.

838

839
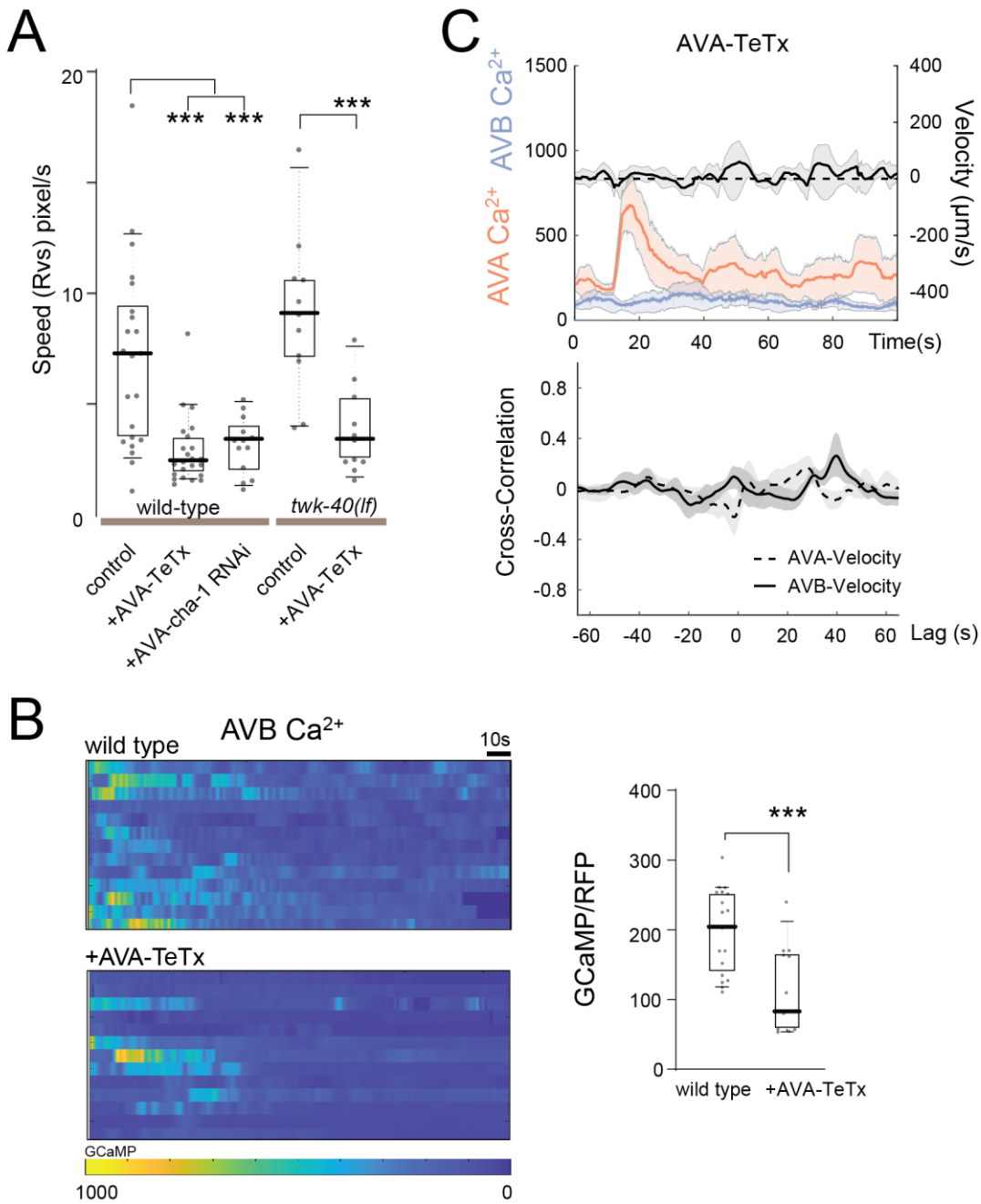
840 **Figure 8S. Chemical synaptic and cholinergic signaling from AVA positively regulates**

841 **overall motor activity**

842 (A) Blocking chemical synaptic transmission from AVA reduces reversal speed. In the wild-type

843 background, AVA-specific expression of TeTx (n=20 animals) resulted in reduced speed during

844 reversals, an effect shared by AVA-specific *cha-1* RNAi transgene (n=14 animals). Wild type

845 control: n=18 animals. In *twk-40(lf)* backward, AVA-specific expression of TeTx also reduced

846 their reversal speed (n=21 animals). when compared to animals without TeTx expression, *twk-*

847 *40(lf)* control: n=14 animals. * denotes statistical significance.

848 (B) Blocking chemical synaptic transmission from AVA reduces AVB calcium activity. Raster plots

849 (left) and quantification (right) of AVB calcium activity in freely moving wild type and AVA-

850 specific TeTx animals. Each line represents one animal. In AVA-specific TeTx animals, overall

851 AVB calcium activity was decreased. n: 20 (wild type), 13 (AVA-specific TeTx).TeTx attenuates

852 AVA's constitutive potentiation on forward movement.

853 (C) Blocking chemical synaptic transmission from AVA disrupts correlations between AVA, AVB,

854 and velocity. (Left) Mean velocity and calcium traces of co-imaged AVA and AVB in freely-

855 moving AVA-specific TeTx animals. (Right) Cross-correlations between AVA calcium and

856 velocity, and AVB calcium and velocity in AVA-specific TeTx animals. n: 19 (wild-type), 10 (AVA-

857 specific TeTx). * denotes statistical significance.

858

859 **Movie S1. Ablation of PVC or RIM in wild-type animals does not change forward**

860 **curvature or disrupt transition between the forward-backward motor states.**

861 Representative movies of freely moving animals with or without ablation of either PVC or RIM

862 neurons. Non ablated refers to wild-type background animals carrying the respective miniSOG

863 transgene for PVC or RIM ablation, but without light exposure. Ablation of PVC or RIM led to

864 increased reversal frequency, but did not change morphological parameters of the forward

865 movement or motor state transition.

866 **Movie S2. Ablation of PVC or RIM in *twk-40(lf)* mutant animals does not reduce**

867 **forward curvature or transitions between the forward-backward motor states.**

868 Representative movies of freely moving animals with or without ablation of either PVC or RIM

869 neurons in *twk-40(lf)* mutants. *twk-40(lf)*; non ablated refers to *twk-40(hp834, lf)* animals

870 carrying the respective miniSOG transgene for PVC or RIM ablation, but without light exposure.

871 Ablation of PVC or RIM did not reduce the extend of forward bending or more frequent motor

872 state transitions.

873

51

874 **Table 1: Membrane potentials of *C. elegans* neurons**

875

Neuron class	Neuron	Approximate 'Rest' MP
Sensory neuron	AFD	-40 mV[99,105], -80 mV[93]
Sensory neuron	AWA	-75 mV[93,106]
Sensory neuron	PLM	-60 mV[98]
Sensory neuron	ASE	-55 mV[37] -60mV[107]
Sensory neuron	ASH	-60 mV[96]
Interneuron	AIY	-55 mV[93]
Interneuron	AIA	-80 mV[108]
Premotor interneuron	AVA	-20 to -30 mV[39,40,66]
Premotor interneuron	AVB	-75 to -55 mV (this study)
Premotor interneuron	AVE	-35 mV (S. Gao, unpublished)
sra-11 expressed neuron	unsure	-20 mV[109]
Motor neuron	RMD	-70 mV and -35 mV[40]
Motor neuron	RIM	-40 mV[93]
Enteric motor neuron	DVB	-60 mV[94]
Enteric motor neuron	AVL	-40 mV[94]
Motor neuron	VA5	-70 mV[41]
Motor neuron	VB6	-50 mV[41]
Motor neuron	VD5	-45 mV[41]

Table 2. Strains and constructs generated and/or used in this study

Strain	Genotype	Constructs	Description (see Notes)	Figures
Electrophysiology recording (visualization of AVA and AVB)				
ZM11177	*hpIs860*	pJH4693	*[Ptwk-40s-eGFP; *Pmyo-2-wCherry]*	1E, F; 1S1A, B; 3C; 3S2A, B
ZM11207	*twk-40(bln336); hpIs860*	pJH4693	*twk-40(gf); [Ptwk-40s-eGFP; *Pmyo-2-wCherry]*	1E, F; 1S1A, B; 3C; 3S2A, B
ZM11208	*twk-40(hp834); hpIs860*	pJH4693	*twk-40(lf); [Ptwk-40s-eGFP; *Pmyo-2-wCherry]*	1E, F; 1S1A, B; 3C; 3S2A, B
***twk-40* mutants and locomotion characterization**				
ZM8302	*twk-40(hp834)*	CRISPR/ Cas9	*twk-40(lf)*	2B, C; 2S1C, D
JIP1514	*twk-40(bln336)*	CRISPR/ Cas9	*twk-40(gf)*	2B, C
JIP1368	*twk-40(bln282)*	CRISPR/ Cas9	*twk-40::TagRFP::ZF*	2S1B, D
ZM10113	*twk-40(bln282); hpIs727*	pJH3830	AVA-specific TWK-40(lf) *twk-40::TagRFP::ZF; [Prig-3-zif-1 sl2 RFP; *Pttx-3-GFP]*	2B, C
ZM10066	*hpEx4053*	pJH4203 pJH2673	AVA- specific TWK-40(gf) *[Prig-3-LoxP stop LoxP twk-40(gf)::GFP; Pnmr-1-Cre]*	2B, C
ZM9662	*twk-40(hp834); hpEx3905*	pJH4019 pJH2673	AVA-specific TWK-40 rescue *twk-40(lf); [Prig-3 FRT Stop FRT twk-40::GFP; Pnmr-1-FLP; *HygR]*	2C
ZM9565	*twk-40(bln282); hpEx3909*	pJH3748	AVA, AVE, AVG-TWK-40(lf) *twk-40::TagRFP::ZF; [Pnmr-1 zif-1 sl2 RFP; *Pttx-3-GFP]*	2S1E
ZM9567	*twk-40(bln282); hpEx3908*	pJH3748	DVC-TWK-40(lf) *twk-40::TagRFP::ZF; [Pceh-63 zif-1 sl2 RFP; *Pttx-3-GFP]*	2S1E
ZM9568	*twk-40(bln282); hpEx3912*	pJH3862	AVA, RIV-TWK-40(lf) *twk-40::TagRFP::ZF; [Pnpr-4 zif-1 sl2 RFP; *Pttx-3-GFP]*	2S1E
ZM9632	*twk-40(bln282); hpEx3889*	pJH3775	AVA, AVB, AVE, SAB, SIA-TWK-40(lf) *twk-40::TagRFP::ZF; [Pglr-5 zif-1 sl2 RFP; *Pttx-3-GFP]*	2S1E
ZM9633	*twk-40(bln282); hpEx3890*	pJH3747	A,B-TWK-40(lf) *twk-40::TagRFP::ZF; [Pacr-2(s) zif-1 sl2 RFP; *Pttx-3-GFP]*	2S1E
ZM9635	*twk-40(bln282); hpEx3891*	pJH3831	AVE-TWK-40(lf) *twk-40::TagRFP::ZF; [Popt-3 zif-1 sl2 RFP; *Pttx-3-GFP]*	2S1E

ZM9641	twk-40(bln282); hpEx3892	pJH3982	TWK-40(lf) all neurons twk-40::TagRFP::ZF; [Prgef-1 zif-1 sl2 eBFP; *Pttx-3-GFP]	2S1E
ZM9646	twk-40(bln282); hpEx3896	pJH4012	A, SAB-TWK-40(lf) twk-40::TagRFP::ZF; [Punc-4 zif-1 sl2 RFP; *Pttx-3-GFP]	2S1E
ZM9645	twk-40(bln282); hpEx3897	pJH4011	AVB-TWK-40(lf) twk-40::TagRFP::ZF; [Plgc-55 zif-1 sl2 RFP; *Pttx-3-GFP]	2S1E
ZM9983	twk-40(bln282); hpEx4034	pJH4034	SIA, SIB-TWK-40(lf) twk-40::TagRFP::ZF; [Pceh-24 zif-1 sl2 RFP; *Pmyo-2-RFP]	2S1E

Immunostaining

ZM10652	twk-40(bln282); hpEx4120	pJH1371	twk-40::TagRFP::ZF; [Prgef-1-GPI::YFP]	1C
ZM9778	twk-40 (hp834); hpIs444	pJH3143	hp834; [twk-40::GFP fosmid]	2S1D

AVA calcium imaging

ZM9059	hpIs580	pJH3631	[Prig-3-GCaMP6s::wCherry; *Lin-15]	1S2A, B
ZM9775	twk-40(hp834); hpIs580	pJH3631	twk-40(lf); [Prig-3-GCaMP6s::wCherry; *Lin-15]	1S2A
ZM9818	twk-40(bln336); hpIs580	pJH3631	twk-40(gf); [Prig-3-GCaMP6s::wCherry; *Lin-15]	1S2A, B
ZM10044	twk-40(hp834); hpIs580; hpEx3905	pJH3631 pJH4019 pJH2673	with AVA-specific TWK-40 rescue twk-40(lf); [Prig-3-GCaMP6::wCherry; *Lin-15] [Prig-3-FRT stop FRT twk-40; Pnmr-1-FLP; *HygR]	1S2A
ZM10283	twk-40(bln282); hpIs580; hpIs727	pJH3631 pJH3830	with AVA-specific TWK-40(lf) twk-40::TagRFP::ZF; [Prig-3-GCaMP6s::wCherry; *Lin-15] [Prig-3-zif-1 sl2 RFP]	2S2C
ZM10346	hpIs580; hpEx4115	pJH3631 pJH4316 pJH4237	with AVA-specific TWK-40(gf) [Prig-3-GCaMP6s::wCherry; *Lin-15] [Pflp-18-LoxP twk-40(gf) LoxP; Ptwk-40s-Cre]	2S2C
ZM8970	nca-1 (hp102); hpIs580	pJH3631	nca-1(gf); [Prig-3-GCaMP6s::wCherry; *Lin-15]	1S2B
ZM10064	nca-1 (hp102); twk-40 (bln336bln282); hpIs580	pJH3631	nca-1(gf); twk-40(gf)::ZF; [Prig-3-GCaMP6s::wCherry; *Lin-15]	1S2B

AVA and A co-ablation

ZM10344	*hpIs371; hpEx4114*	pJH2843 pJH4315 pJH4237	AVA/A miniSOG [Punc-4- mito::miniSOG sl2 mCherry]; [Pflp-18-LoxP stop LoxP mito::miniSOG sl2 mCherry; Ptwk-40s-Cre]	2S2A
ZM11234	*twk-40(hp834); hpIs371; hpEx4114*	pJH2843 pJH4315 pJH4237	twk-40(lf); [Punc-4-mito::miniSOG sl2 mCherry]; [Pflp-18-LoxP stop LoxP mito::miniSOG sl2 mCherry; Ptwk-40s-Cre]	2S2A
PVC ablation				
ZM7054	*hpIs321*	pJH2827	AVA, AVE, AVD, RIM, PVC mini SOG [Pnmr-1-tomm-20::miniSOG sl2 Cherry]	3S1A
RIM ablation				
ZM7978	*hpIs327*	pJH2829	RIM miniSOG [Pcex-1-tomm-20::miniSOG sl2 Cherry]	3S1A
AVA-specific TeTx and *cha-1* RNAi				
ZM10755	*hpIs814*	pJH4508 pJH4237	AVA-specific TeTx [Pflp-18-LoxP Stop LoxP TeTx::cherry; Ptwk-40s-Cre]	8A; 8SA-C
ZM11082	*twk-40 (hp834) ; hpIs814*	pJH4508 pJH4237	twk-40(lf); [Pflp-18-LoxP Stop LoxP TeTx::cherry; Ptwk-40s-Cre]	8A; 8SA-C
ZM11086	*hpEx4362*	PCR product	AVA-specific *cha-1* RNAi [Pflp-18-cha-1(sense); Ptwk-40-cha-1 (antisense); *Pttx-3-GFP]	8A, 8SA
AVA peptide secretion and synaptic vesicle analyses				
ZM11039	*hpEx4351*	pJH4677	[Pnpr-4-ins-22::GFP]	7C
ZM11078	*hpEx4351; hpEx4364*	pJH4677 pJH4506	with AVA-TeTx [Pnpr-4-ins-22::GFP]; [Pnpr-4-TeTx]	7C
ZM11084	*hpEx4363*	pJH4687	[Pnpr-4-ins-22::pHluorin]	7B
ZM11085	*hpEx4363; hpIs814*	pJH4687 pJH4508 pJH4237	with AVA-TeTx [Pnpr-4-ins-22::pHluorin]; [Pflp-18-LoxP Stop LoxP TeTx::cherry; Ptwk-40s-Cre]	7B
ZM10040	*hpIs721*	pJH4169 pJH2673	AVA-specific vesicle marker [Prig-3 FRT stop FRT SNB-1::GFP; Pnmr-1-FLP]	7A
ZM10786	*hpIs721; hpIs811*	pJH4169 pJH2673 pJH4508 pJH4237	with AVA-TeTx [Prig-3 FRT stop FRT SNB-1::GFP; Pnmr-1-FLP]; [Pflp-18-LoxP Stop LoxP TeTx::cherry; Ptwk-40s-Cre]	7A

AVA optogenetic (Chrimson) activation				
ZM10206	*hpIs758*	pJH4253 pJH4237	*[Prig-3-LoxP Stop LoxP Chrimson::Cherry; Ptwk-40s-Cre]*	6B
ZM11151	*hpIs758;* *hpIs814*	pJH4253 pJH4237 pJH4508 pJH4237	with AVA-TeTx *[Prig-3-LoxP Stop LoxP Chrimson::Cherry; Ptwk-40s-Cre];* *[Pflp-18-LoxP Stop LoxP TeTx::wCherry; Ptwk-40s-Cre]*	8B
AVA HisCl chemogenetic inactivation				
ZM9354	*hpIs636*	Ref.[32]	*[Prig-3::HisCl1::SL2::mCherry]*	6C, D
ZM11286	*hpIs636;* *hpEx4479*	Ref.[32] pJH4783	*[Prig-3::HisCl1::SL2::mCherry];* *[Pnpr-4-SNB-1::pHluorin]*	6E
ZM11287	*hpEx4479*	pJH4783	*[Pnpr-4-SNB-1::pHluorin]*	6F
ZM11284	*twk-40(bln336);* *hpEx4479*	 pJH4783	*twk-40(gf);* *[Pnpr-4-snb-1::pHluorin]*	6F
ZM11285	*twk-40 (hp834);* *hpEx4479*	 pJH4783	*twk-40(lf);* *[Pnpr-4-snb-1::pHluorin]*	6F
AVA optogenetic (GtACR2) inactivation				
ZM10806	*hpIs824*	pJH4562 pJH4237	*[Pflp-18-LoxPStopLoxP gtACR2::wCherry; Ptwk-40s-Cre]*	2S2B
ZM10538	*hpIs774;* *hpEx4081*	pJH4293 pJH4217 pJH4237	with AVA/AVB co-calcium imaging *[Ptwk-40s-GCaMP6s::mNeptune]* *[Prig-3 LoxP Stop LoxPgtACR2::wCherry; Ptwk-40s-Cre]*	4B, D 4SB, D
AVB optogenetic (GtACR2) inactivation				
ZM10942	*hpIs774;* *hpEx4292*	pJH4293 pJH4609 pJH4237	with AVA/AVB co-calcium imaging *[Ptwk-40s-GCaMP6s::mNeptune];* *[Ppdf-1 LoxP eBFP LoxP gtACR2::Cherry; Ptwk-40s-Cre]*	4A, C 4SA, C
AVB ablation				
ZM7297	*hpIs331*	pJH2890	AVB miniSOG *[Plgc-55-mito::miniSOG UrSL wCherry]*	3A; 3S1A, B
ZM10327	*twk-40(bln282);* *hpIs331;* *hpIs727*	 pJH2890 pJH3830	with AVA-specific TWK-40(lf) *twk-40::TagRFP::ZF;* *[Plgc-55-mito::miniSOG UrSL wCherry];* *[Prig-3-zif-1 sl2 RFP]*	3B
ZM10683	*hpIs331;* *hpIs768*	pJH2890 pJH4316 pJH4237	with AVA-specific TWK-40(gf) *[Plgc-55-mito::miniSOG UrSL wCherry];* *[Pflp-18-LoxP twk-40(gf)::GFP LoxP; Ptwk-40-Cre]*	3S1B

56

ZM11173	hpIs331; hpIs758	pJH2890 pJH4253 pJH4237	with AVA-specific Chrimson [Plgc-55-mito::miniSOG UrSL wCherry]; [Prig-3-LoxPStopLoxP Chrimson::Cherry; Ptwk-40s-Cre]	6SA
ZM11172	hpIs331; hpIs824	pJH2890 pJH4562 pJH4237	with AVA-specific GtACR2 [Plgc-55-mito::miniSOG UrSL wCherry]; [Pflp-18-LoxP Stop LoxP gtACR2::Cherry; Ptwk-40s-Cre]	3S1C
AVA-AVB co-calcium imaging				
ZM10767	hpIs819	pJH4542	[Ptwk-40s-GCaMP T2A nls::mNeptune]	3D; 5B-D; 5SA-D
ZM11014	twk-40(bln282); hpIs819; hpEx3904	pJH4542 pJH4018 pJH2673	with AVA-specific TWK-40(lf) twk-40::TagRFP::ZF; [Ptwk-40s-GCaMP T2A nls::mNeptune]; [Prig-3 FRT zif-1 sl2 eBFP FRT; Pnmr-1-FLP; *HygR]	3D; 5B-D; 5SA, B-D
ZM11015	hpIs819; hpIs768	pJH4542 pJH4316 pJH4237	with AVA-specific TWK-40(gf) [Ptwk-40s-GCaMP T2A nls::mNeptune]; [Pflp-18-LoxP twk-40(gf)::GFP LoxP; Ptwk-40s-Cre]	3D; 5E, F; 5SA, D
ZM11034	hpIs819; hpIs810	pJH4542 pJH4508 pJH4237	AVA-specific TeTx [Ptwk-40s-GCaMP T2A nls::mNeptune]; [Pflp-18-LoxP TeTx::wCherry LoxP; Ptwk-40s-Cre]	8C; 8SA-C
Notes: [ ] integrated or extra-transgenic arrays; * Co-injection markers; Stop: stop codon or termination sequence in the let-858 3' UTR.				

878

Methods

Constructs and strains

See Supplemental Table for a full list of constructs and stains used in this study. Primers and sequences are available upon request. All *C. elegans* strains were cultured on the standard Nematode Growth Medium (NGM) plates seeded with OP50 and maintained at 22.5 °C unless specified. The wild-type animal refers to the Bristol N2 strain or animals. The control animal refers to a transgenic line without explicitly introduced genetic mutations. L4 stage hermaphrodites were used for the experiments unless specified otherwise.

Isolation, cloning, and generation of *twk-40* mutants

The first loss of function allele of *twk-40(hp733)* was isolated in a genetic screen based on altered behavior. *hp733* was isolated with exaggerated amplitude in both forward and reverse movement as well as a tendency to form a backward coil. *hp733* was mapped to the left arm of chromosome III past the SNP marker W06F12 at ~-21. Whole genome sequencing was performed, and a single missense mutation (E36K) was identified in t*wk-40*. Fosmids and plasmids containing wild-type *twk-40* coding sequence fully rescued the behavioral change in *hp733*. Subsequently, we generated another loss of function allele in *twk-40(hp834)* using CRISPR gene editing. *hp834* has a 7bp deletion in between exon 1 and the following intron (at base 3378-3384 (GTTCGAG) of T28A8.1b), resulting in a frame-shift mutation of *twk-40* that expresses only the first twelve amino acids of the channel. *hp834* displayed similar but stronger behavioral defects than *hp733* and was easy to be genotyped. We subsequently used *hp834* as the canonical *lf* allele for all experiments shown in this study.

Gain of function allele *bln336, L181N* was engineered by CRISPR/Cas9 editing by mutating the 4298-4299 base of T28A8.1b from CT to AA[49]. TWK-40 degradation was generated by a repurposed E3 ligase degradation system[51]. *bln282 (twk-40::TagRFP::ZF)* was generated by CRISPR/Cas9 genome editing to insert an in frame TagRFP::ZF fusion at base pair 5785 at T28A8.1b (*twk-40*)[101].

AVA-specific TWK-40(lf) was generated by expressing ZIF in AVA using the *rig-3* promoter or *nmr-1/rig-3*-promoter combination (*Prig-3 FRT zif-1 sl2 eBFP FRT; Pnmr-1-FLP*) via the FRT-FLP recombination system in *bln282 (twk-40::TagRFP::ZF)* background. AVA-specific TWK-40(gf) was generated by expressing TWK-40(L181N)::GFP in AVA by *flp-18/twk-40*-promoter combination (*Pflp-18-LoxP stop LoxP twk-40(gf)::GFP; Ptwk-40-cre*) or via the Cre-LoxP recombination system in the N2 background, or *rig-3/nmr-1* promoter combination (*Prig-3-LoxP stop LoxP twk-40(gf)::GFP; Pnmr-1-Cre*) via the FRT-FLP recombination system in N2 background. AVA-specific TWK-40 rescue was generated by expressing TWK-40(WT)::GFP in AVA by *rig-3/nmr-1*-promoter combination (*Prig-3 FRT Stop FRT twk-40::GFP; Pnmr-1-FLP*) via the Cre-LoxP recombination system in *twk-40(lf)* background.

Spontaneous locomotion analyses

A single L4 animal was collected and transferred to an NGM plate with a thin layer of evenly spread OP50. After 30 seconds, it was recorded on a tracking microscope using an in-house developed ImageJ plugin[26]. A 3-minute movie of the animals was recorded at 10 fps. At least 10 animals for each genotype were recorded on the same day using the same condition. The movies were analyzed as previously described[26,58]. Briefly, the animal contour was divided into 33 segments by its centerline along the longitudinal axis. Body curvature in radian between adjacent body segment segments (5-32) was calculated. Velocity was calculated by the displacement of the centroid.

Electrophysiology

Exogenous TWK-40 channel whole-cell patch recording in HEK293 cells: HEK293 cells were cultured in the DMEM medium with 10% fetal bovine serum, 1% double antibody at 5% CO_2, and 37°C. TWK-40 expression construct was generated by RT-PCR amplification of cDNA b isoform and inserting into the BstXI and NheI sites of the pCDNA3.1 vector. After 24 hours of transfection of the plasmid with the liposome ExFect2000 (Vazyme, China), cells were patched using 4-6 MΩ-resistant borosilicate pipettes (1B100F-4, World Precision Instruments, USA). Pipettes were pulled by micropipette puller P-1000 (Sutter, USA), and fire-polished by microforge MF-830 (Narishige, Japan). Membrane currents and I-V curve were recorded and plotted in the whole-cell configuration by pulse software with the EPC-9 amplifier (HEKA, Germany) and processed with the Igor Pro (WaveMetrics, USA) and Clampfit 10 software (Axon Instruments, Molecular Devices, USA). I-V curve was recorded at a holding potential from –80 mV to 80 mV with 20 mV step voltages. Data were digitized at 10-20 kHz and filtered at 2.6 kHz. The pipette solution contained (in mM): KCl 140; $MgCl_2$ 1; EGTA 10; HEPES 10; Na_2ATP 4; pH 7.3 with KOH, ~300 mOsm. The bath solution consisted of (in mM): NaCl 140; KCl 3.6; $CaCl_2$ 2.5; $MgCl_2$ 1; pH 7.3 with NaOH, ~310 mOsm. For low intracellular K^+ recording, the pipette solution contained (in mM): KCl 14; CsCl 126; $MgCl_2$ 1; EGTA 10; HEPES 10; Na_2ATP 4; pH 7.3 with CsOH, ~300 mOsm. Chemicals were obtained from Sigma unless stated otherwise. Experiments were performed at room temperatures (20-22°C).

in situ whole-cell patch clamp of C. elegans neurons AVA and AVB: Premotor interneuron whole-cell patch clamp recording was performed using a strain with fluorescent labeling of AVA and AVB neurons, a configuration as previously described[26,39], which was modified from previous reports[40,44,110]. Briefly, 1- or 2-day-old hermaphrodite adults were glued (Histoacryl Blue, Braun) to a sylgard-coated cover glass covered with bath solution (Sylgard 184, Dowcorning) under a stereoscopic microscope (M50, Leica). After clearing the viscera by suction through a glass pipette, the cuticle flap was turned and gently glued down using WORMGLU (GluStitch Inc.) to expose the soma of AVA and AVB neurons. Neurons were patched using ~20 MΩ-resistant borosilicate pipettes (1B100F-4; World Precision Instruments). Pipettes were pulled by micropipette puller P-1000 (Sutter) and fire-polished by microforge MF-830 (Narishige). Membrane currents and potentials were collected in the whole-cell

955 configuration by pulse software with an EPC9 amplifier (HEKA, Germany). Data were digitized at
956 10 kHz and filtered at 2.6 kHz. The recording pipette solution consisted of: KCl 25 mM; K-
957 Gluconate 115 mM; CaCl$_2$ 0.1 mM; MgCl$_2$ 5 mM; BAPTA 1 mM; HEPES 10 mM; Na$_2$ATP 5 mM;
958 Na$_2$GTP 0.5 mM; cAMP 0.5 mM; cGMP 0.5 mM, pH 7.2 with KOH, ~320 mOsm. cGMP and cAMP
959 were included to increase the longevity of the preparation[39,111]. The bath solution consisted of
960 KCl 5 mM; NaCl 150 mM; CaCl$_2$ 5 mM; MgCl$_2$ 1 mM; glucose 10 mM; sucrose 5 mM; HEPES 15
961 mM, pH 7.3 with NaOH, ~330 mOsm. The K$^+$ current was recorded at a holding potential from –
962 60 mV and followed a ramp voltage stimulation from –90 mV to 90 mV. The membrane voltage
963 recording was performed at 0 pA for at least 30 seconds. The background leak currents were
964 recorded at –60 mV. Healthy preparations were selected based on the following criteria: whole-
965 cell capacitance (1-1.5 pF), and steady-state leak current (–20-0 pA at –60mV). Experiments
966 were performed at room temperatures (20-22°C).

Cell ablation by MiniSOG

968 Strains expressing miniSOG[112] in AVB, RIM, AVA, A, or AVA/A were used for ablation by
969 exposing L2 larvae to blue LED light as described in previous studies[25,58,113]. Briefly, cells
970 expressing miniSOG were co-labeled with RFP. animals were treated with 30-40 min LED blue
971 light using a homemade device and allowed to recover for 1 day. L4 animals were recorded for
972 behavioral analyses. For PVC ablation, L2-stage transgenic animals that express miniSOG in
973 multiple premotor interneurons, including but not exclusive to PVC, were anesthetized by
974 sodium azide and mounted on a 2 percent agarose pad with a coverslip. The tail region was
975 exposed to a blue laser for 30 min and animals were allowed to recover for 2 days before
976 recording at the L4 stage. Only healthy animals were recorded and analyzed. The ablation
977 efficiency was confirmed by the disappearance or distortion of the soma fluorescence and
978 fragmentation of neurites.

Optogenetic stimulation for behavioral and calcium imaging

980 *Strains:* Strains that express AVA-specific Chrimson or GtACR2 strains were used for AVA-
981 specific stimulation and inhibition, respectively. The specificity of AVA-specific GtACR2 was
982 verified by AVA ablation using *Pnmr-1*-miniSOG. The AVA-ablated animal no longer exhibited
983 light-induced inhibition during forward and backward movement. Transgenic animals were
984 cultured on ATR plates in darkness for two generations. The second-generation L4-stage
985 animals were analyzed for behavior and calcium activities. Controls were animals of the same
986 genotypes, cultured and treated similarly, except with no ATR included on culture plates.

987 *Behaviors upon stimulation*: an individual L4-stage animal was transferred to an imaging plate
988 with a thin layer of evenly spread OP50. After 30 seconds, the movement of the animal was
989 tracked during multiple stimulation cycles: 10s pre-stimulation, 10s stimulation, 10s post-
990 stimulation; or, 30 seconds pre-stimulation, 30 seconds stimulation, and 30 seconds post-
991 stimulation. 488nm and 574nm LED light stimulation were applied to inhibit and activate AVA,
992 by activating GtACR2 and Chrimson, respectively.

Constitutive, minimal Chrimson-mediated AVA activation: ATR-supplemented NGM plates were seeded with regular OP50 supplemented with ATR (1ml OP50/0.5μl 50μm ATR). Animals were cultured on ATR plates for at least 1 day for behavior recording. Before recording, animals were conditioned with 544nm green LED light for up to 5min (Zeiss V16), followed by recording at 595nm yellow light (Thorlabs) at low intensity (4 out of 63 A.U.).

Minimal GtACR2-mediated AVA inactivation: Animals were cultured on ATR-supplemented NGM plates for at least 1 day for behavior recording. During stimulation, animals were exposed to 470nm blue LED light at low intensity (4 out of 63 A.U.).

GtACR2-mediated AVB inactivation: L4 stage AVB-specific GtACR2 animals were incubated on plates with or without -ATR or +ATR (1ml OP50 /5μl 50μM ATR) plates for 2 hours and then subjected to behavior recording with a constant 470nm LED exposure at low intensity (4 out of 63 A.U.) for 800 seconds.

Simultaneous calcium recording and optogenetic stimulation: The experiment process was previously described[113]. Briefly, L4 stage animals carrying AVA and AVB calcium reporters and either AVA-specific GtACR2 or AVB-specific GtACR2 were incubated on -ATR or +ATR plates for 2 hours. They were immobilized on dry agarose pads in M9 buffer and subjected to full spectrum light illumination for simultaneous calcium imaging and GtACR2-mediated inhibition at 10 fps or 20 pfs for 6-20 seconds.

Behavioral analyses upon chemogenetic manipulation

Animals of the L4 stage carrying an extrachromosomal array for *Prig-3* HisCl::mCherry[32] were incubated on 0mM, 2mM, 5mM, or 10mM histamine plates with OP50 for 1 hour before being individually placed on the behavioral imaging plates for spontaneous behavior recording and quantification.

Immunofluorescent staining and imaging

Mixed stages of animals with endogenously tagged *twk-40* (*twk-40*::TagRFP::ZF), with or without the plasma marker (*Prgef*-1-GPI::YFP), and animals with an integrated *twk-40::GFP* fosmid were fixed in 2% paraformaldehyde at 4°C for 1 hour and processed as previously described[114]. Primary antibodies against TagRFP (Thermo Fisher Scientific, R10367, rabbit) and/or GFP (Roche, mouse) were used at 1:500 and 1:200 dilution, respectively. Secondary antibodies of goat-anti-rabbit (Alexa Fluor 488) and/or goat anti-mouse (Alexa Fluor 594) were used at 1:5000 dilution. L4 larvae and adults were imaged with a Nikon spinning disk confocal microscope with a 63x objective and reconstructed by maximum intensity projection. Single layers of acquired images from animals co-expressing TWK-40::TagRFP::ZF and GPI::YFP were examined for subcellular colocalization using an ImageJ plugin (JACoP).

Live fluorescence microscopy of GFP and pHluorin

Live L4 larvae were immobilized on dry agarose pads in a small drop of M9 buffer. Fluorescence signals were captured using Nikon Eclipse 90i confocal microscope and Nikon Eclipse T12 with

1030 Yokogawa CSU-X1 spinning disk field scanning confocal system. For pHluorin imaging, all images
1031 were acquired within 10min after dry pad preparation. All fluorescent images were analyzed by
1032 the in-house developed puncta analyzer[115] or ImageJ intensity analyzer.

Calcium imaging of premotor interneurons in moving animals

1034 AVA (L or R) or AVB (L or R) single neuron imaging was performed in L4 larvae as previously
1035 described[73]. Briefly, an individual transgenic animal was placed on a 2.5 percent agarose pad to
1036 ensure its slow movement. The animal was allowed to recover for 3min and then recorded
1037 using Zeiss Axioskop 2 Plus upright microscope with 40x objective or Nikon spinning disc
1038 confocal with 20x objective in the wide-field mode. Signal extraction and calcium activity
1039 (GCaMP/RFP ratio unless stated otherwise) were carried out as previously described[113].

1040 For AVA (L or R) and AVB (L or R) co-imaging, an individual transgenic L4 stage animal
1041 expressing the GCaMP6s calcium sensor in AVA and AVB (*hpIs819*) was mounted on a 2 percent
1042 NGM gel pad with ~1µl M9 buffer so that it could move under a coverslip. Mounted animals
1043 were allowed to recover for 3min on the pad before recording. The recording was performed
1044 using a 20x objective on Nikon spinning disk confocal microscope. Animals were centered in the
1045 field of view by manual tracking. AVB soma was manually kept in focus at the RFP channel
1046 during recording. The initiation of each epoch of reversal to forward locomotion transition was
1047 defined by the alignment between velocity and AVA-AVB calcium activity (GCaMP intensity)
1048 using in-house-developed MATLAB scripts[113].

Cell-specific perturbation of neurotransmission

1050 AVA-specific TeTx was achieved by the Cre-LoxP recombination system. AVA-specific *cha-1*
1051 RNAi was generated using the combination of P*flp-18* and P*twk-40* promoter combination to
1052 drive the sense and anti-sense strands of *cha-1* genomic DNA, respectively. The following
1053 primers and templates were used: (A) P*flp-18*: OZM6199 (GATGGATACGCTAACAACTTGG) and
1054 OZM6200 (CTACAACGGCAGCGTATTCGATCCCGTCTAAC-CCTGAAA) amplified from pJH4631. (B)
1055 *cha-1* exon: OZM6201 (GAATACGCTGCCGTTGTAG) and OZM6240
1056 (GTCGAGTGCTCTATGCACAACC), amplified from N2 genomic DNA. (C) P*twk-40s*: OZM6199
1057 (GATGGATACGCTAACAACTTGG) and OZM6253 (GTATGATGCGACTATTCAGCTGT-
1058 GAATATTCATCACTCGATATTCCA) amplified from pJH4608. (D) *cha-1* exon: OZM6201
1059 (GAATACGCTGCCGTTGTAG) and OZM6202 (CAGCTGAATAGTCGCATCATAC), amplified from N2
1060 genomic DNA. PCR fusion was performed to obtain sense and anti-sense *cha-1* by following
1061 primers: *Pflp-18-cha-1*(sense): OZM6203 (AGCTTAGCCGGAATAGGGTCA) and OZM6202
1062 (CAGCTGAATAGTCGCATCATAC), amplified from mixed PCR product (A+B). Ptwk-40-cha-
1063 1(antisense): OZM3543 (AATGCGGCCGCTCTAATCACTATCACGT GGGATCTGGATAA); OZM6254
1064 (CGTAG-GCCAGAAAGCCTCAC) from mixed PCR product (C+D). Mixed PCR products were
1065 injected into N2 animals.

1066 **Modeling**

1067 Our approach is to find the simplest phenomenological model (i.e. a non-mechanistic model
1068 with as few free parameters as possible) that explains the observed calcium activity patterns of
1069 AVA and AVB, as opposed to a detailed, more biologically realistic model. A more realistic
1070 model will have several parameters, the estimation of which will require assumptions or
1071 experiments to fix.

1072 We first note that our experiments suggest that the communication between AVB and AVA is
1073 largely unidirectional, with AVA affecting AVB's activity and very little effect in the opposite
1074 direction. Consequently, we start with the following equation for the calcium activity of AVB,
1075 x_{AVB}

1076
$$\frac{dx_{AVB}}{dt} = -\frac{1}{\tau_{AVB}} \cdot x_{AVB} + \sigma(w_{AVA} \cdot x_{AVA} + \Sigma_i w_i z_i + c)$$
1077

1078 Where x_{AVA} is the calcium activity of AVA, z_i is the activity of all other input neurons of AVB, w_i
1079 is the synaptic weight of each input, c is the bias input, and σ denotes the activation function
1080 for the dynapse. Typically, the activation function is a sigmoidal function. However, to simplify
1081 the model we restrict our attention to the linear case, where σ is simply the identity function,
1082 $\sigma(x) = x$.

1083 Next, we make a key simplification to the model above based on our experiments. Our results
1084 show that AVA forms the dominant input on to AVB. Specifically, AVA-twk-40(gf) animals
1085 cannot sustain their forward motion (Fig. 2B) and AVB's calcium is significantly reduced in this
1086 background (Fig. 3D). This suggests that we can ignore the input from other neurons in the
1087 model. Thus, we set $w_i = 0$ for all neurons other than AVA. Giving us the following leaky-
1088 integrator differential equation.

1089

1090
$$\frac{1}{w_{AVA}}\frac{dx_{AVB}}{dt} = -\frac{1}{\tau_{AVB} \cdot w_{AVA}} \cdot x_{AVB} + x_{AVA} + c$$
1091

1092 As a final simplification, we assume that the direct input from AVA is faster than the kinetics of
1093 the calcium sensor, such that any activity in AVA is immediately reflected in AVB. Thus, we
1094 consider the limit $\frac{1}{w_{AVA}} \to 0$. Giving us the final simplified model as,

1095
$$x_{AVB} = a \cdot x_{AVA} + c$$

1096 Where $a = \frac{1}{\tau_{AVB} \cdot w_{AVA}}$ is a dimensionless multiplier. As seen in Fig. 5B, this model with $a < 0$
1097 (black dotted line) can predict the anticorrelated activity pattern between AVA and AVB during
1098 a reversal, but is unable to explain AVB's activity after the reversal.

1099

63

1100   To capture the slow decay of AVB, we add an additional slower input from AVA to AVB (as
1101   shown in the schematic in Fig. 5A). Giving us the following system of equations with just three
1102   free parameters.

1103
$$x_{AVB} = a \cdot x_{AVA} + b \cdot y$$
1104

1105
$$\frac{dy}{dt} = -\frac{1}{\tau} \cdot y + x_{AVA}$$

1106   Where, a and b are the coefficients for the fast and slow inputs respectively, and τ is the
1107   integration time-constant for the slow component of AVA. To fit the parameters from calcium
1108   imaging data, we used *procest* function from MATLAB's system identification toolbox, which
1109   estimates the transfer function for the equation above. Laplace transforming the system of
1110   equations above results in the following transfer function,

1111

1112
$$\frac{X_{AVB}(s)}{X_{AVA}(s)} = \left[\frac{(a + b \cdot \tau) + (a \cdot \tau) \cdot s}{1 + \tau \cdot s}\right]$$

1113

1114   which has one zero and one pole. The number of zeros and poles form the input to *procest*,
1115   along with the calcium traces of AVB calcium (set as output signal) and AVA calcium (set as the
1116   input signal). To get a distribution over model parameters and performances, we do a cross-
1117   validation procedure where the parameters are estimated from a single recording and then
1118   tested on the remaining recordings. The model R-squared showed in Fig 5C shows the
1119   distribution from the models thus estimated.

1120   The same setup was used to model the velocity from AVA's calcium activity (Fig 5G) using
1121   *procest* (i.e. a single pole, single zero transfer function), with AVA's activity being set as the
1122   input signal and velocity forming the output signal.

1123   **Statistical analyses**

1124   *Electrophysiological analyses:* The cumulative distributions for the membrane voltage of AVA
1125   and AVB were calculated using MATLAB's *ecdf* function. To compute the joint histogram (Fig.
1126   1S1, Fig. 3S2), we first computed the derivative of membrane potential with a finite difference
1127   (preceded by smoothing with a Gaussian kernel) and then used MATLAB's bivariate histogram
1128   *histogram2* to perform the histogram estimation. For HEK293 cell recording, the Mann-
1129   Whitney U tests were used.

1130   *Behavior and fluorescent analysis:* Mann-Whitney U tests were used to quantify data of box and
1131   whisker plots unless stated otherwise.

1132   *Calcium imaging*: Error bars in Fig. 4 and Fig. 4S were computed as a 95% confidence interval of
1133   the mean bootstrapped over 1000 resamples.

1134   P value less than 0.05 is considered to be statistically significant. *: $P < 0.05$, **: $P < 0.01$, ***: P
1135   <0.001.

Conflict of interests

1137   The authors declare no conflict of interest.

Author contributions

1139   Conception and supervision: MZ; Design of experiments, modeling, and analyses: JM, TA, WH,
1140   SG, TB, MZ; Data collection: JM, TA, BY, WH, ZY, SM, SG; Reagents and scripts: SM, ZW, YZ, TA,
1141   QW; MJ, TA, and MZ wrote the manuscript; all authors edited or approved the manuscript.

Acknowledgments

References

1. Carreira-Rosario, A. *et al.* MDN brain descending neurons coordinately activate backward and inhibit forward locomotion. *Elife* **7**, (2018).

2. Briggman, K. L. & Kristan, W. B. Imaging dedicated and multifunctional neural circuits generating distinct behaviors. *J. Neurosci.* **26**, 10925–10933 (2006).

3. Mazzucato, L. Neural mechanisms underlying the temporal organization of naturalistic animal behavior. *Elife* **11**, (2022).

4. Briggman, K. L. & Kristan, W. B. Multifunctional pattern-generating circuits. *Annual Review of Neuroscience* **31**, 271–294 (2008).

5. Ramirez, J. M. & Pearson, K. G. Generation of motor patterns for walking and flight in motoneurons supplying bifunctional muscles in the locust. *J. Neurobiol.* **19**, 257–282 (1988).

6. Roberts, W. M. *et al.* A stochastic neuronal model predicts random search behaviors at multiple spatial scales in C. elegans. *Elife* **5**, (2016).

7. Berkowitz, A. Both shared and specialized spinal circuitry for scratching and swimming in turtles. *J. Comp. Physiol. A. Neuroethol. Sens. Neural. Behav. Physiol.* **188**, 225–234 (2002).

8. Gaudry, Q., Ruiz, N., Huang, T., Kristan, W. B. & Kristan, W. B. Behavioral choice across leech species: chacun à son goût. *J. Exp. Biol.* **213**, 1356–1365 (2010).

9. Koyama, M. *et al.* A circuit motif in the zebrafish hindbrain for a two alternative behavioral choice to turn left or right. *Elife* **5**, (2016).

10. Popescu, I. R. & Frost, W. N. *Highly Dissimilar Behaviors Mediated by a Multifunctional Network in the Marine Mollusk Tritonia diomedea*. *Soc Neuroscience* (2002).

11. Soffe, S. R. Two distinct rhythmic motor patterns are driven by common premotor and motor neurons in a simple vertebrate spinal cord. *J. Neurosci.* **13**, 4456–4469 (1993).

12. Itti, L. & Koch, C. Computational modelling of visual attention. *Nat. Rev. Neurosci.* **2**, 194–203 (2001).

13. Goodhill, G. J. Contributions of theoretical modeling to the understanding of neural map development. *Neuron* **56**, 301–311 (2007).

14. Kohonen, T. Self-organized formation of topologically correct feature maps. *Biol. Cybern.* **43**, 59–69 (1982).

15. Lynch MIT, N., Musco, C. & Parter, M. Winner-Take-All Computation in Spiking Neural Networks. (2019). doi:10.48550/arxiv.1904.12591

16. Chen, Y. Mechanisms of winner-take-all and group selection in neuronal spiking networks. *Front. Comput. Neurosci.* **11**, 20 (2017).

17. Szigeti, B., Deogade, A. & Webb, B. Searching for motifs in the behaviour of larval Drosophila melanogaster and Caenorhabditis elegans reveals continuity between behavioural states. *J. R. Soc. Interface* **12**, (2015).

18. Stephens, G. J., Johnson-Kerner, B., Bialek, W. & Ryu, W. S. Dimensionality and dynamics in the behavior of C. elegans. *PLoS Comput. Biol.* **4**, (2008).

19. Gomez-Marin, A., Stephens, G. J. & Brown, A. E. X. Hierarchical compression of Caenorhabditis elegans locomotion reveals phenotypic differences in the organization of behaviour. *J. R. Soc. Interface* **13**, (2016).

1192 20. Ahamed, T., Costa, A. C. & Stephens, G. J. Capturing the continuous complexity of
1193   behaviour in Caenorhabditis elegans. *Nat. Phys.* **17**, 275–283 (2021).

1194 21. Lindén, H., Petersen, P. C., Vestergaard, M. & Berg, R. W. Movement is governed by
1195   rotational neural dynamics in spinal motor networks. *Nat. 2022 6107932* **610**, 526–531
1196   (2022).

1197 22. Croll, N. A. Components and patterns in the behaviour of the nematode Caenorhabditis
1198   elegans. *J. Zool.* **176**, 159–176 (1975).

1199 23. White, J., Southgate, E. & Thomson, J. The structure of the nervous system of the
1200   nematode Caenorhabditis elegans. *Trans R Soc L. B Biol …* (1986).

1201 24. Chen, B. L., Hall, D. H. & Chklovskii, D. B. Wiring optimization can relate neuronal
1202   structure and function. *Proc. Natl. Acad. Sci. U. S. A.* **103**, 4723–4728 (2006).

1203 25. Gao, S. *et al.* Excitatory motor neurons are local oscillators for backward locomotion.
1204   *Elife* **7**, (2018).

1205 26. Kawano, T. *et al.* An imbalancing act: Gap junctions reduce the backward motor circuit
1206   activity to bias C. elegans for forward locomotion. *Neuron* **72**, 572–586 (2011).

1207 27. Xu, T. *et al.* Descending pathway facilitates undulatory wave propagation in
1208   Caenorhabditis elegans through gap junctions. *Proc. Natl. Acad. Sci. U. S. A.* **115**, E4493–
1209   E4502 (2018).

1210 28. Fang-Yen, C., Alkema, M. J. & Samuel, A. D. T. Illuminating neural circuits and behaviour
1211   in *Caenorhabditis elegans* with optogenetics. *Philos. Trans. R. Soc. B Biol. Sci.* **370**,
1212   20140212 (2015).

1213 29. Chalfie, M. *et al.* The neural circuit for touch sensitivity in Caenorhabditis elegans. *J.
1214   Neurosci.* **5**, 956–964 (1985).

1215 30. Meng, J. Molecular , Cellular and Circuit Mechanisms that underlie a Two-pore Potassium
1216   C hannel ' s Regulation of Membrane Potential , Synaptic Activity and Locomotion
1217   Molecular , Cellular and Circuit Mechanisms that underlie a Two-pore Potassium C
1218   hannel ' s Reg. (University of Toronto, 2022).

1219 31. Rodgers, J. B. & Ryu, W. S. Targeted thermal stimulation and high-content phenotyping
1220   reveal that the C. elegans escape response integrates current behavioral state and past
1221   experience. *PLoS One* **15**, (2020).

1222 32. Pokala, N., Liu, Q., Gordus, A. & Bargmann, C. I. Inducible and titratable silencing of
1223   Caenorhabditis elegans neurons in vivo with histamine-gated chloride channels. *Proc.
1224   Natl. Acad. Sci.* **111**, 2770–2775 (2014).

1225 33. Faumont, S. *et al.* An Image-Free Opto-Mechanical System for Creating Virtual
1226   Environments and Imaging Neuronal Activity in Freely Moving Caenorhabditis elegans.
1227   *PLoS One* **6**, e24666 (2011).

1228 34. Husson, S. J., Gottschalk, A. & Leifer, A. M. Optogenetic manipulation of neural activity in
1229   C. elegans: From synapse to circuits and behaviour. *Biology of the Cell* **105**, 235–250
1230   (2013).

1231 35. Schmitt, C., Schultheis, C., Husson, S. & Liewald, J. Specific expression of
1232   channelrhodopsin-2 in single neurons of Caenorhabditis elegans. *PLoS One* (2012).

1233 36. Gao, S. *et al.* The NCA sodium leak channel is required for persistent motor circuit activity
1234   that sustains locomotion. *Nat. Commun.* **6**, 6323 (2015).

1235 37. Goodman, M. B., Hall, D. H., Avery, L. & Lockery, S. R. Active currents regulate sensitivity

1236   and dynamic range in C. elegans Neurons. *Neuron* **20**, 763–772 (1998).

1237   38.   Goodman, M. B., Lindsay, T. H., Lockery, S. R. & Richmond, J. E. Electrophysiological
1238   Methods for C. elegans Neurobiology. *Methods Cell Biol.* **107**, 409 (2012).

1239   39.   Xie, L. *et al.* NLF-1 Delivers a Sodium Leak Channel to Regulate Neuronal Excitability and
1240   Modulate Rhythmic Locomotion. *Neuron* **77**, 1069–1082 (2013).

1241   40.   Mellem, J., Brockie, P., Madsen, D. & Maricq, A. Action potentials contribute to neuronal
1242   signaling in C. elegans. *Nat. Neurosci.* (2008).

1243   41.   Liu, P., Chen, B. & Wang, Z.-W. SLO-2 potassium channel is an important regulator of
1244   neurotransmitter release in Caenorhabditis elegans. *Nat. Commun. 2014 51* **5**, 1–12
1245   (2014).

1246   42.   Huang, Y. C. *et al.* Gain-of-function mutations in the UNC-2/CaV2α channel lead to
1247   excitation-dominant synaptic transmission in C. elegans. *Elife* **8**, (2019).

1248   43.   Saheki, Y. & Bargmann, C. I. Presynaptic CaV2 calcium channel traffic requires CALF-1 and
1249   the alpha(2)delta subunit UNC-36. *Nat. Neurosci.* **12**, 1257–1265 (2009).

1250   44.   Richmond, J. E. & Jorgensen, E. M. One GABA and two acetylcholine receptors function at
1251   the C. elegans neuromuscular junction. *Nat. Neurosci.* **2**, 791–798 (1999).

1252   45.   Oh, K. H., Krout, M. D., Richmond, J. E. & Kim, H. UNC-2 CaV2 Channel Localization at
1253   Presynaptic Active Zones Depends on UNC-10/RIM and SYD-2/Liprin-α in Caenorhabditis
1254   elegans. *J. Neurosci.* **41**, 4782–4794 (2021).

1255   46.   Lesage, F. TWIK-1, a ubiquitous human weakly inward rectifying K+ channel with a novel
1256   structure. *EMBO J.* **15**, 1004–1011 (1996).

1257   47.   Cluzeaud, F. *et al.* Expression of TWIK-1, a novel weakly inward rectifying potassium
1258   channel in rat kidney. *Am. J. Physiol. - Cell Physiol.* **275**, (1998).

1259   48.   Chavez, R., Gray, A., Zhao, B. & Kindler, C. TWIK-2, a new weak inward rectifying member
1260   of the tandem pore domain potassium channel family. *J. Biol.* (1999).

1261   49.   Ben Soussia, I. *et al.* Mutation of a single residue promotes gating of vertebrate and
1262   invertebrate two-pore domain potassium channels. *Nat. Commun.* **10**, 1–13 (2019).

1263   50.   Aryal, P., Abd-Wahab, F., Bucci, G. & Sansom, M. A hydrophobic barrier deep within the
1264   inner pore of the TWIK-1 K2P potassium channel. *Nature* (2014).

1265   51.   Armenti, S. T., Lohmer, L. L., Sherwood, D. R. & Nance, J. Repurposing an endogenous
1266   degradation system for rapid and targeted depletion of C. elegans proteins. *Dev.* **141**,
1267   4640–4647 (2014).

1268   52.   Zheng, Y., Brockie, P. J., Mellem, J. E., Madsen, D. M. & Maricq, A. V. Neuronal control of
1269   locomotion in C. elegans is modified by a dominant mutation in the GLR-1 ionotropic
1270   glutamate receptor. *Neuron* **24**, 347–361 (1999).

1271   53.   Pirri, J. K., McPherson, A. D., Donnelly, J. L., Francis, M. M. & Alkema, M. J. A Tyramine-
1272   Gated Chloride Channel Coordinates Distinct Motor Programs of a Caenorhabditis
1273   elegans Escape Response. *Neuron* **62**, 526–538 (2009).

1274   54.   Ji, N. *et al.* Corollary discharge promotes a sustained motor state in a neural circuit for
1275   navigation. *Elife* **10**, (2021).

1276   55.   Gordus, A., Pokala, N., Levy, S., Flavell, S. W. & Bargmann, C. I. Feedback from network
1277   states generates variability in a probabilistic olfactory circuit. *Cell* **161**, 215–227 (2015).

1278   56.   Wagh, D. A. *et al.* Bruchpilot, a protein with homology to ELKS/CAST, is required for
1279   structural integrity and function of synaptic active zones in Drosophila. *Neuron* **49**, 833–

1280   844 (2006).

1281 57. Sordillo, A. & Bargmann, C. I. Behavioral control by depolarized and hyperpolarized states
1282   of an integrating neuron. *Elife* **10**, (2021).

1283 58. Chitturi, J. *et al.* The UBR-1 ubiquitin ligase regulates glutamate metabolism to generate
1284   coordinated motor pattern in Caenorhabditis elegans. *PLOS Genet.* **14**, e1007303 (2018).

1285 59. Fouad, A. D. *et al.* Distributed rhythm generators underlie Caenorhabditis elegans
1286   forward locomotion. *Elife* **7**, (2018).

1287 60. Kato, S. *et al.* Global Brain Dynamics Embed the Motor Command Sequence of
1288   Caenorhabditis elegans. *Cell* **163**, 656–669 (2015).

1289 61. Kindt, K. S. *et al.* Dopamine Mediates Context-Dependent Modulation of Sensory
1290   Plasticity in C. elegans. *Neuron* **55**, 662–676 (2007).

1291 62. Nguyen, J. P. *et al.* Whole-brain calcium imaging with cellular resolution in freely
1292   behaving *Caenorhabditis elegans*. *Proc. Natl. Acad. Sci.* **113**, E1074–E1081 (2016).

1293 63. N, J. *et al.* Corollary discharge promotes a sustained motor state in a neural circuit for
1294   navigation. *Elife* **10**, (2021).

1295 64. Ben Arous, J., Tanizawa, Y., Rabinowitch, I., Chatenay, D. & Schafer, W. R. Automated
1296   imaging of neuronal activity in freely behaving Caenorhabditis elegans. *J. Neurosci.*
1297   *Methods* **187**, 229–234 (2010).

1298 65. Venkatachalam, V. *et al.* Pan-neuronal imaging in roaming Caenorhabditis elegans. *Proc.*
1299   *Natl. Acad. Sci. U. S. A.* **113**, E1082–E1088 (2016).

1300 66. Liu, P., Chen, B., Mailler, R. & Wang, Z. W. Antidromic-rectifying gap junctions amplify
1301   chemical transmission at functionally mixed electrical-chemical synapses. *Nat. Commun.*
1302   **8**, 1–16 (2017).

1303 67. Starich, T. A., Xu, J., Skerrett, I. M., Nicholson, B. J. & Shaw, J. E. Interactions between
1304   innexins UNC-7 and UNC-9 mediate electrical synapse specificity in the Caenorhabditis
1305   elegans locomotory nervous system. *Neural Dev. 2009 41* **4**, 1–28 (2009).

1306 68. Bhardwaj, A., Thapliyal, S., Dahiya, Y. & Babu, K. FLP-18 functions through the G-protein-
1307   coupled receptors NPR-1 and NPR-4 to modulate reversal length in Caenorhabditis
1308   elegans. *J. Neurosci.* **38**, 4641–4654 (2018).

1309 69. Taylor, S. R. *et al.* Molecular topography of an entire nervous system. *Cell* **184**, 4329-
1310   4347.e23 (2021).

1311 70. Hammarlund, M., Hobert, O., Miller, D. M. & Sestan, N. The CeNGEN Project: The
1312   Complete Gene Expression Map of an Entire Nervous System. *Neuron* **99**, 430–433
1313   (2018).

1314 71. Hoogstraaten, R. I., van Keimpema, L., Toonen, R. F. & Verhage, M. Tetanus insensitive
1315   VAMP2 differentially restores synaptic and dense core vesicle fusion in tetanus
1316   neurotoxin treated neurons. *Sci. Rep.* **10**, (2020).

1317 72. Schiavo, G. G. *et al.* Tetanus and botulinum-B neurotoxins block neurotransmitter release
1318   by proteolytic cleavage of synaptobrevin. *Nat. 1992 3596398* **359**, 832–835 (1992).

1319 73. Lim, M. A. *et al.* Neuroendocrine modulation sustains the C. elegans forward motor state.
1320   *Elife* **5**, (2016).

1321 74. Hammell, C. M. & Hannon, G. J. Inducing RNAi in Caenorhabditis elegans by Injection of
1322   dsRNA. *Cold Spring Harb. Protoc.* **2016**, 80–85 (2016).

1323 75. Ghezzi, A., Liebeskind, B. J., Thompson, A., Atkinson, N. S. & Zakon, H. H. Ancient

1324 association between cation leak channels and Mid1 proteins is conserved in fungi and
1325 animals. *Front. Mol. Neurosci.* **7**, (2014).

76. Zhao, B., Khare, P., Feldman, L. & Dent, J. A. Reversal Frequency in Caenorhabditis
elegans Represents an Integrated Response to the State of the Animal and Its
Environment. *J. Neurosci.* **23**, 5319 (2003).

77. Pierce-Shimomura, J. T., Morse, T. M. & Lockery, S. R. The Fundamental Role of
Pirouettes in Caenorhabditis elegans Chemotaxis. *J. Neurosci.* **19**, 9557 (1999).

78. Gray, J. M., Hill, J. J. & Bargmann, C. I. A circuit for navigation in Caenorhabditis elegans.
Proc. Natl. Acad. Sci. U. S. A. **102**, 3184–3191 (2005).

79. CROLL, N. A. Components and patterns in the behaviour of the nematode Caenorhabditis
elegans. *J. Zool.* **176**, 159–176 (2009).

80. Chen, L. *et al.* Escape steering by cholecystokinin peptidergic signaling. *Cell Rep.* **38**,
(2022).

81. Huang, K. M., Cosman, P. & Schafer, W. R. Machine vision based detection of omega
bends and reversals in C. elegans. *J. Neurosci. Methods* **158**, 323–336 (2006).

82. Wang, Y. *et al.* Flexible motor sequence generation during stereotyped escape responses.
Elife **9**, 1–27 (2020).

83. Mohammadi, A., Byrne Rodgers, J., Kotera, I. & Ryu, W. S. Behavioral response of
Caenorhabditis elegans to localized thermal stimuli. *BMC Neurosci.* **14**, (2013).

84. Cook, S. J. *et al.* Whole-animal connectomes of both Caenorhabditis elegans sexes.
Nature **571**, 63–71 (2019).

85. Witvliet, D. *et al.* Connectomes across development reveal principles of brain
maturation. *Nature* **596**, 257–261 (2021).

86. Lu, Y. *et al.* Extrasynaptic signaling enables an asymmetric juvenile motor circuit to
produce symmetric undulation. *Curr. Biol.* **32**, 4631-4644.e5 (2022).

87. Kaplan, H. S., Salazar Thula, O., Khoss, N. & Zimmer Correspondence, M. Nested
Neuronal Dynamics Orchestrate a Behavioral Hierarchy across Timescales. *Neuron* **105**,
562-576.e9 (2020).

88. Randi, F., Sharma, A. K., Dvali, S. & Leifer, A. M. A functional connectivity atlas of
$\textit{C. elegans}$ measured by neural activation. (2022).
doi:10.48550/arxiv.2208.04790

89. Ashaber, M. *et al.* Anatomy and activity patterns in a multifunctional motor neuron and
its surrounding circuits. *Elife* **10**, 1–30 (2021).

90. Takahashi, N., Sasaki, T., Matsumoto, W., Matsuki, N. & Ikegaya, Y. Circuit topology for
synchronizing neurons in spontaneously active networks. *Proc. Natl. Acad. Sci. U. S. A.*
107, 10244–10249 (2010).

91. Wang, Z. *et al.* The relationship of anatomical and functional connectivity to resting state
connectivity in primate somatosensory cortex. *Neuron* **78**, 1116 (2013).

92. Zarin, A. A., Mark, B., Cardona, A., Litwin-Kumar, A. & Doe, C. Q. A multilayer circuit
architecture for the generation of distinct locomotor behaviors in Drosophila. *Elife* **8**,
(2019).

93. Liu, Q., Kidd, P. B., Dobosiewicz, M. & Bargmann, C. I. C. elegans AWA Olfactory Neurons
Fire Calcium-Mediated All-or-None Action Potentials. *Cell* **175**, 57-70.e17 (2018).

94. Jiang, J. *et al.* C. elegans enteric motor neurons fire synchronized action potentials

1368   underlying the defecation motor program. *Nat. Commun. 2022 131* **13**, 1–15 (2022).

1369   95.   Liu, Q., Hollopeter, G. & Jorgensen, E. M. Graded synaptic transmission at the
1370   Caenorhabditis elegans neuromuscular junction. *Proc. Natl. Acad. Sci. U. S. A.* **106**,
1371   10823–10828 (2009).

1372   96.   Geffeney, S. L. *et al.* DEG/ENaC but not TRP channels are the major mechanoelectrical
1373   transduction channels in a C. elegans nociceptor. *Neuron* **71**, 845 (2011).

1374   97.   Lindsay, T. H., Thiele, T. R. & Lockery, S. R. Optogenetic analysis of synaptic transmission
1375   in the central nervous system of the nematode Caenorhabditis elegans. *Nat. Commun.* **2**,
1376   306 (2011).

1377   98.   O'Hagan, R., Chalfie, M. & Goodman, M. B. The MEC-4 DEG/ENaC channel of
1378   Caenorhabditis elegans touch receptor neurons transduces mechanical signals. *Nat.*
1379   *Neurosci.* **8**, 43–50 (2005).

1380   99.   Ramot, D., MacInnis, B. L. & Goodman, M. B. Bidirectional temperature-sensing by a
1381   single thermosensory neuron in C. elegans. *Nat. Neurosci.* **11**, 908–915 (2008).

1382   100.   Salkoff, L., Wei, A., Baban, B., Butler, A. & Fawcett, G. Potassium channels in C. elegans.
1383   (2005).

1384   101.   El Mouridi, S. *et al.* Reliable CRISPR/Cas9 genome engineering in Caenorhabditis elegans
1385   using a single efficient sgRNA and an easily recognizable phenotype. *G3 Genes, Genomes,*
1386   *Genet.* **7**, 1429–1437 (2017).

1387   102.   Genome sequence of the nematode C. elegans: a platform for investigating biology.
1388   *Science* **282**, 2012–2018 (1998).

1389   103.   Salkoff, L. *et al.* Evolution tunes the excitability of individual neurons. *Neuroscience* **103**,
1390   853–859 (2001).

1391   104.   Zhou, C. *et al.* Differential modulation of C. elegans motor behavior by NALCN and two-
1392   pore domain potassium channels. *PLoS Genet.* **18**, (2022).

1393   105.   Goodman, M. B. & Sengupta, P. The extraordinary AFD thermosensor of C. elegans.
1394   *Pflugers Arch.* **470**, 839 (2018).

1395   106.   Nicoletti, M. *et al.* Biophysical modeling of C. Elegans neurons: Single ion currents and
1396   whole-cell dynamics of AWCon and RMD. *PLoS One* **14**, e0218738 (2019).

1397   107.   Shindou, T. *et al.* Active propagation of dendritic electrical signals in C. elegans. *Sci.*
1398   *Reports 2019 91* **9**, 1–12 (2019).

1399   108.   Dobosiewicz, M., Liu, Q. & Bargmann, C. I. Reliability of an interneuron response depends
1400   on an integrated sensory state. *Elife* **8**, (2019).

1401   109.   Faumont, S., Lindsay, T. & Lockery, S. Neuronal microcircuits for decision making in C.
1402   elegans. *Curr. Opin. Neurobiol.* **22**, 580–591 (2012).

1403   110.   Richmond, J. E., Davis, W. S. & Jorgensen, E. M. Unc-13 is required for synaptic vesicle
1404   fusion in C. elegans. *Nat. Neurosci.* **2**, 959–964 (1999).

1405   111.   Brockie, P. J., Mellem, J. E., Hills, T., Madsen, D. M. & Maricq, A. V. The C. elegans
1406   Glutamate Receptor Subunit NMR-1 Is Required for Slow NMDA-Activated Currents that
1407   Regulate Reversal Frequency during Locomotion. *Neuron* **31**, 617–630 (2001).

1408   112.   Qi, Y., Garren, E. & Shu, X. Photo-inducible cell ablation in Caenorhabditis elegans using
1409   the genetically encoded singlet oxygen generating protein miniSOG. *Proc.* (2012).

1410   113.   Lu, Y. *et al.* Extrasynaptic signaling enables an asymmetric juvenile motor circuit to
1411   produce symmetric undulation. *Curr. Biol.* **0**, (2022).

1412   114.   Meng, J. *et al.* Myrf ER-bound transcription factors drive C. elegans synaptic plasticity via
1413   cleavage-dependent nuclear translocation. *Dev. Cell* **41**, 180 (2017).
1414   115.   Yeh, E., Kawano, T., Weimer, R. M., Bessereau, J. L. & Zhen, M. Identification of Genes
1415   Involved in Synaptogenesis Using a Fluorescent Active Zone Marker in Caenorhabditis
1416   elegans. *J. Neurosci.* **25**, 3833 (2005)
1417